COMPUTATIONAL MECHANOBIOLOGY MODEL EVALUATING HEALING OF POSTOPERATIVE CAVITIES FOLLOWING BREAST-CONSERVING SURGERY

by

Zachary Harbin

A Thesis

Submitted to the Faculty of Purdue University

In Partial Fulfillment of the Requirements for the degree of

Master of Science in Mechanical Engineering

School of Mechanical Engineering

West Lafayette, Indiana

May 2023

THE PURDUE UNIVERSITY GRADUATE SCHOOL
STATEMENT OF COMMITTEE APPROVAL

Dr. Adrian Buganza Tepole, Chair

Department of Mechanical Engineering

Dr. Taeyoon Kim

Weldon School of Biomedical Engineering

Dr. Hector Gomez

Department of Mechanical Engineering

Approved by:

Dr. Nicole Key

Dedicated to my family, friends, colleagues, and everyone who has helped and supported me throughout the years.

ACKNOWLEDGMENTS

This work would not have been possible without all of the mentors and coworkers that I have had. I would first like to thank my advisor, Dr. Adrian Buganza Tepole, for his mentorship during my three years working alongside him. Between this work and the two finite element classes I have taken from you, I have learned so much about mathematical modeling and its vast applications. This has only grown my passion for this space, and your belief in me along the way has been deeply appreciated. I would also like to thank my committee members, Dr. Taeyoon Kim and Dr. Hector Gomez, for their mentorship and guidance as well.

This work would also not be possible without the help and support of the members of the Buganza Tepole lab and the Voytik-Harbin lab. Specifically, I would like to thank Dr. Sherry Voytik-Harbin for her contributions to the project and the passion that she brings every day. I would also like to thank the two graduate mentors that I have had throughout the years, Dr. David Sohutskay and Dr. Emma Vanderlaan, who have assisted and guided me since I have been an undergraduate student. You both have had a great impact on the engineer that I have become today. I would also like to thank Muira Fontaine and Carly Mendenhall, who are two students that I worked alongside during my time as an undergraduate student on this project. Finally, I would also like to thank Dr. Carla Fisher, the Director of Breast Surgical Oncology at IU Health, for all her time and contributions to the preclinical porcine lumpectomy study. All of these people have contributed significantly to the work in this thesis, including Chapter 3, which is a manuscript that is currently in preparation for submission for publication.

This work was supported by NSF CMMI grant (A.B.T.; 1911346) and NSF SBIR Phase I award (S.V.-H.; 1913626).

TABLE OF CONTENTS

LIST OF TABLES

LIST OF FIGURES

LIST OF SYMBOLS

ρ	Fibroblast Density
c	Cytokine Density
ϕ	Collagen Density
$p_{\rho,c}$	Cytokine-Increased Proliferation
$d_{\rho,\phi}$	Fibroblast Diffusion Scaling Constant
$v_\rho(\phi)$	Fibroblast Speed
Δ	Skewness of Fibroblast Speed $v_\rho(\phi)$
p_ϕ	Collagen Production
$p_{\phi,c}$	Collagen Production Activated by Cytokine
t_ρ	Contractile Force of Fibroblasts
$t_{\rho,c}$	Contractile Force of Myofibroblasts
τ_{λ^p}	Rate of Plastic Deformation
D_c	Cytokine Diffusion Coefficient
$d_{\rho,c}$	Cytokine-Increased Fibroblast Diffusivity
$d_{\rho,0}$	Baseline Fibroblast Diffusivity
p_ρ	Fibroblast Proliferation
$K_{\rho,c}$	Proliferation Saturation due to Cytokine
$p_{\rho,\mathrm{e}}$	Mechanoregulation of Fibroblast Proliferation
$K_{\rho,\rho}$	Fibroblast Division Saturation
d_ρ	Fibroblast Death Rate
$p_{c,\rho}$	Fibroblast Secretion of Cytokine
$p_{c,\mathrm{e}}$	Mechanoregulation of Cytokine
$K_{c,c}$	Cytokine Saturation
d_c	Cytokine Death Rate
ρ_0	Nominal Fibroblast Density
c_0	Initial Cytokine Concentration Inside Cavity
ϕ_0	Nominal Collagen Density
k_0	Linear Stiffness

K_1	Compressibility
k_f	Fiber Stiffness
k_2	Nonlinear Stiffening
γ_{e}	Shape of Mechanosensing Curve
ϑ_{e}	Midpoint of Mechanosensing Curve
$K_{t,c}$	Traction Saturation due to Cytokine
$K_{\phi,c}$	Collagen Production Saturation due to Cytokine
$p_{\phi_{\mathrm{e}}}$	Collagen Production Activated by Stretch
$K_{\phi,\rho}$	Collagen Production Saturation due to Collagen Fraction
d_ϕ	Collagen Degradation
$d_{\phi,c}$	Collagen Degradation Activated by Cytokine
τ_ω	Time Constant for Reorientation
τ_κ	Time Constant for Dispersion
γ_κ	Shape of Dispersion Rate Curve
Γ	Boundary
φ	Deformation Mapping
β_0	Reference Configuration
β_t	Time-Dependent Configuration
κ	Fiber Dispersion
a_0	Principal Collagen Alignment Vector
s_0	In-Plane Orthogonal Alignment Vector
n_0	Out-of-Plane Orthogonal Alignment Vector
F	Deformation Gradient
F^{e}	Elastic Deformation Gradient
F^p	Plastic Deformation Gradient
λ_a^p	Principal Stretch in Direction a_0
λ_s^p	Principal Stretch in Direction s_0
λ_n^p	Principal Stretch in Direction n_0
Q_ρ	Fibroblast Flux Term

Q_c	Cytokine Flux Term
s_ρ	Fibroblast Source Term
s_c	Cytokine Source Term
$H(J^{\mathrm{e}})$	Mechanosensing Logistic Function
σ	Stress
σ^{act}	Active Stress
σ^{pas}	Passive Stress
Ψ	Strain Energy Function
I_1^{e}	First Elastic Invarient
I_4^{e}	Fourth Elastic Invarient
J^{e}	Elastic Volume Change
λ^{crit}	Plastic Deformation Threshold
λ_1	Largest Eigenvalue
e_1	Largest Eigenvector
Θ_b	Biochemical GP Parameters
Θ_m	Mechanobiological GP Parameters
V_t	Cavity Volume at Time t
E_{BT}	Young's Modulus of Breast Tissue
E_{Fat}	Young's Modulus of Fat Tissue
$E_{Fibroglandular}$	Young's Modulus of Fibroglandular Tissue
υ	Poisson's Ratio

ABBREVIATIONS

BCS	Breast-Conserving Surgery
GP	Gaussian Process
1D	One-Dimensional
2D	Two-Dimensional
3D	Three-Dimensional
SSO	Society of Surgical Oncology
ASTRO	American Society of Radiation Oncology
ASCO	American Society of Clinical Oncology
TBVP	Tumor to Breast Volume Percentage
BI-RADS	Breast Imaging Reporting and Data System
MRI	Magnetic Resonance Imaging
PDE	Partial Differential Equation
RMSE	Root Mean Square Error
CBVP	Cavity to Breast Volume Percentage
ECM	Extracellular Matrix
EBVP	Excision to Breast Volume Percentage
BMI	Body Mass Index
FE	Finite Element
TGF-β	Transforming Growth Factor Beta
PDGF	Platelet-Derived Growth Factor

ABSTRACT

Breast cancer is the most commonly diagnosed cancer type worldwide. Given high survivorship, increased focus has been placed on long-term treatment outcomes and patient quality of life. While breast-conserving surgery (BCS) is the preferred treatment strategy for early-stage breast cancer, anticipated healing and breast deformation (cosmetic) outcomes weigh heavily on surgeon and patient selection between BCS and more aggressive mastectomy procedures. Unfortunately, surgical outcomes following BCS are difficult to predict, owing to the complexity of the tissue repair process and significant patient-to-patient variability. To overcome this challenge, we developed a predictive computational mechanobiological model that simulates breast healing and deformation following BCS. The coupled biochemical-biomechanical model incorporates multi-scale cell and tissue mechanics, including collagen deposition and remodeling, collagen-dependent cell migration and contractility, and tissue plastic deformation. Available human clinical data evaluating cavity contraction and histopathological data from an experimental porcine lumpectomy study were used for model calibration. The computational model was successfully fit to data by optimizing biochemical and mechanobiological parameters through the Gaussian Process. The calibrated model was then applied to define key mechanobiological parameters and relationships influencing healing and breast deformation outcomes. Variability in patient characteristics including cavity-to-breast volume percentage and breast composition were further evaluated to determine effects on cavity contraction and breast cosmetic outcomes, with simulation outcomes aligning well with previously reported human studies. The proposed model has the potential to assist surgeons and their patients in developing and discussing individualized treatment plans that lead to more satisfying post-surgical outcomes and improved quality of life.

1. INTRODUCTION

1.1 Background and Significance

Breast cancer is one of the most prevalent cancers affecting women today, with approximately 287,850 women in the United States alone being diagnosed in 2022 [1]. Fortunately, advancements in treatment technology and screening awareness have allowed for the breast cancer death rate to decline 43% in the past 30 years [2]. To date, the 5-year survival rate is reported to be 90.6%, allowing for more attention to go toward bettering long-term quality of life for patients after BCS [2]. For treatment, the current standard of care is breast-conserving surgery (BCS; otherwise known as lumpectomy) paired with whole breast radiation therapy [3]. Surgeons performing BCS aim to preserve healthy breast tissue, excising only the tumor along with a small margin of healthy tissue. This forms a breast tissue cavity that undergoes the wound healing process leading to tissue contraction, scar formation, and breast deformation. The alternative procedure is mastectomy, which is the removal of the whole breast. However, patients who undergo mastectomy report worse cosmetic results and lower quality of life compared to BCS patients [4]. Furthermore, BCS has similar/improved survival and recurrence rates while also having decreased risks of surgical complications [5]–[8].

The choice of surgical procedure is a collaborative effort between the breast cancer patient and their surgeon. This decision-making process can ultimately be challenging, multi-faceted, and stressful due to the large number of unknowns associated with both options. Specifically, treatment choice is typically weighed by surgeons based on the expected cosmetic result, as good aesthetic outcomes are associated with patient psychological recovery and quality of life [9], [10]. However, the complexity of the tissue repair process along with variations in patient, tumor, and treatment-related factors make it extremely challenging, if not impossible, for surgeons to predict healing, oncologic, and cosmetic outcomes of BCS. Specifically, it has been reported that age, health status, breast size and consistency, tumor size and location, and adjunct radiation or chemotherapy all factor into the final cosmetic result [11]. With these characteristics commonly intertwined, a predictive tool is needed to better understand the mechanistic interplay between the contributing factors. Furthermore, the inability to predict healing outcomes also stems from the complex interplay of biochemical and biome-

chanical processes during wound healing. Therefore, it is important to accurately represent mechanobiological aspects of the tissue repair process.

The wound healing response is made up of four overlapping phases: hemostasis, inflammation, proliferation, and remodeling. This process is generally described for cutaneous wound healing, however, a breast cavity is repaired through similar methods [12]. One noted difference is that the tissue cavity left after BCS is fully enclosed, which is unlike superficial skin wounds which have an air-tissue interface. For breast cavities, hemostasis begins often through the creation of a blood clot (hematoma) and/or serous fluid building up inside the cavity. Platelets are deposited within an initial fibrin scaffold that has limited mechanical integrity. However, it does allow for local tissue contracture while promoting inflammation and cellularization. The degranulation of platelets causes cytokine secretion, releasing agents such as TGF-β or PDGF that are chemotactic for neutrophils and macrophages. These inflammatory cells clean and eliminate pathogens, tissue debris, or other invading microorganisms. The formation of a cytokine gradient within the cavity also promotes the proliferation and migration of fibroblasts and endothelial cells into the wound space. Fibroblasts and actively differentiated myofibroblasts break down the provisional fibrin scaffold and deposit collagen to help build up the structural and mechanical framework of the extracellular matrix (ECM). With this, fibroblasts and myofibroblasts exert a traction force on the ECM, contracting the scaffold and realigning the collagen fibers. In turn, this causes the creation of dense, stiff scar tissue within the contracted cavity. The process of scar formation and remodeling takes place over an extended period of time, as the scar tissue properties evolve, but never become as strong as healthy tissue.

The remodeling of the lost tissue and scar formation is the most unpredictable aspect of healing following BCS. It has been reported that 15%-30% of BCS patients experience hypertrophic scarring and severe contraction post-lumpectomy, which commonly results in breast deformities and altered breast consistency [13]–[16]. Denting, scarring, and breast asymmetry are all poor cosmetic outcomes that women may face for the rest of their lives, which can negatively impact women emotionally and psychologically [17]. This results in a large portion of women turning to additional reconstructive surgery after undergoing BCS [18], [19]. Along the same lines, some patients and patients elect to use oncoplastic procedures

and techniques, such as breast reshaping, volume displacement, or breast reduction while the patient is having the tumor removed [20]. However, these methods are limited due to the increased medical costs and the need for an extra surgeon with specialized training [21], [22].

To date, there are currently very few standard surgical tools that exist to help surgeons preoperatively plan and predict oncologic and cosmetic outcomes. Instead, their judgment is often dependent on the surgeons past training and experience. Past efforts have been made in creating surgical decision models to help recommend treatment thresholds (i.e., when to treat a patient with BCS versus mastectomy) based on tumor size and location [13], [23], [24]. These models are developed based on correlative analyses of human BCS patient data, including tumor-to-breast volume percentage, tumor location, quality of life surveys, and cosmetic outcome assessments [13], [23], [24]. Furthermore, two separate groups have also aimed to develop computational tools with the goal of simulating breast cavity healing after BCS and predicting post-surgical breast deformation. The creation of surgical computational tools has been a relatively new field with the goal of accurately modeling the patients mechanobiological response to the procedure [25]. Garbey et al. (2013) proposed the framework for a two-dimensional (2D) multi-scale model that was used in later work to simulate patient-specific breast deformations by calibrating the model to fit one-dimensional (1D) Magnetic Resonance Imaging (MRI) profiles [26], [27]. In 2016, Vavourakis et al. developed a three-dimensional (3D) mechanobiological finite element model with an underlying framework adapted from a prior cutaneous wound model [28]. Utilizing MRI data, they were able to evaluate time-dependent wound healing while further validating the model by comparing post-surgical surface scans to predictive simulations [28]. For these current computational models, both lack an experimentally informed, descriptive mechanobiological wound healing response. Although both modeling efforts implement nonlinear breast tissue mechanics, they lack complex descriptions of tissue growth and remodeling. These areas are especially important to capture, as the breast cavity will undergo large deformations and permanent remodeling throughout the wound healing process, which is coupled with cellular activity.

1.2 Organization of Thesis

For the work presented in this thesis, we address the gap by presenting the framework for a computational mechanobiological model that aims to assist surgeons in creating individualized treatment plans that better predict oncologic, healing, and cosmetic outcomes following BCS. The coupled biochemical-biomechanical model focuses on multi-scale mechanics, including large plastic deformation, cell contractility, and collagen remodeling. Through this, the specific aim of the model was to use available preclinical and clinical data to calibrate the model while also evaluating model parameters and patient-specific characteristics to find their effects on breast healing and post-surgical cosmetic outcomes.

Following this introductory chapter, Chapter 2 details our initial efforts of adapting the computational model that was fit for dermal wound repair and making it specific for healing following BCS. Human clinical data from the literature was used to inform characteristics such as breast tissue material properties, breast tissue composition, and cavity location. Due to the extensive amount of information available about cavity contraction after irradiation instead of directly after surgery, a unique generalized breast geometry reflective of these studies was created. This allowed for the calibration of mechanobiological parameters by fitting the model to this data using a machine learning technique known as the Gaussian Process.

Chapter 3 represents a manuscript that is in preparation for submission for publication. It builds upon the work by informing the biochemical portion of the model through histological data from an experimental porcine lumpectomy study to find time-dependent changes in fibroblast and collagen density. This allowed for further model calibration by optimizing biochemical parameters to fit experimental fibroblast and collagen data through the Gaussian Process. Further, the model was also fit to cavity contraction data that was reflective of the wound healing process directly after surgery by tuning mechanobiological parameters. The optimized model allowed us to give insight into how model parameters and patient-specific characteristics contribute to post-surgical deformation and cosmetic outcomes.

Chapter 4 concludes this work with a discussion about the significance of our findings and the next steps for the model. This project betters the mechanistic understanding of the

breast healing process by effectively simulating fibroblast infiltration, collagen remodeling, and breast permanent deformation. Although previous models of wound healing after BCS have been developed, we advanced these efforts by implementing a detailed mechanobiological model coupled with the nonlinear mechanics of breast tissue, including large plastic deformation and collagen remodeling. This knowledge has the potential to help surgeons better develop individualized patient treatment plans that lead to decreased post-surgical complications, decreased surgical procedures (e.g., re-excision, revision, and/or reconstruction), and improved patient satisfaction and quality of life.

2. ADAPTATION OF A COMPUTATIONAL MECHANOBIOLOGICAL CUTANEOUS WOUND MODEL TO EVALUATE HEALING FOLLOWING BREAST-CONSERVING SURGERY

2.1 Motivation

Breast cancer is one the most prevalent cancer in women today, with approximately 287,500 new cases in the United States each year [1]. Although there have been a high number of cases, fatality rates have decreased dramatically throughout the past few decades, allowing the 5-year survival rate to be 90.6% [2]. This can be attributed to the higher frequency of breast cancer testing along with the improvement in surgical technique and screening technology.

In recent years, breast-conserving surgery (BCS; otherwise known as lumpectomy) has replaced mastectomy (the removal of the entire breast) as the preferred standard of care for breast cancer. This procedure better preserves the healthy breast tissue, as surgeons make an excision to only remove the breast tumor along with a small margin of healthy breast tissue surrounding the tumor. As the excision is closed, this leaves a tissue cavity inside the breast. The void slowly heals over time through the wound healing process, with four overlapping phases: hemostasis, inflammatory, proliferative, and remodeling. Directly after the surgery is the hemostasis stage, in which a blood clot and/or seroma builds inside the cavity. Inflammatory cells cause the formation of a cytokine gradient within the cavity, which, in turn, promotes fibroblast proliferation and migration into the wound space. Fibroblasts and actively differentiated myofibroblasts are further guided by collagen deposition, fiber realignment, and scaffold contraction, creating stiff scar tissue within the contracted cavity. The remodeling stage continues this process over an extended period of time, as the collagen network is built back to form scar tissue that has weaker mechanical properties compared to healthy tissue.

As a result of the cavity and the wound healing process, there are potential negative oncologic and cosmetic outcomes that are difficult for surgeons to predict before surgery.

The patient-to-patient variability exacerbates this problem due to variations in breast size, tissue composition, and tumor geometry and location. Approximately 30% of patients who undergo BCS report having poor cosmetic outcomes, which can potentially be damaging to the patients self-image and quality of life [13], [17]. These outcomes can vary from hypertrophic scarring, dents/deformation in the breast, or breast asymmetry.

To overcome these challenges, we are developing a predictive computational mechanobiology model that simulates patient-specific breast healing following BCS.. The creation of surgical computational models has been a relatively new field, aiming to model the patients biological response to the procedure [25]. These tools have the potential to be used alongside surgeons to better predict oncologic and cosmetic outcomes of BCS, allowing for patient-specific treatment plans. To date, there have been two other known computational models that aimed to simulate the lumpectomy cavity [26], [28]. Both models utilized patient-specific breast and cavity geometries informed by imaging data (e.g., magnetic resonance and/or surface). While the models do incorporate biochemical signaling to simulate the wound healing response, they lack complex descriptions of tissue growth and remodeling. The goal of our model is to simulate a unique generalized breast geometry that better captures large deformations through collagen deposition and remodeling using a coupled biochemical and enhanced biomechanical model.

In this work, we look to transform and adapt a computational model that was fit to simulate cutaneous wound healing and make it breast-specific. This was done by performing an extensive literature review to create a generalized breast geometry and inform breast material properties, breast composition, and tumor/cavity location. Clinical data depicting the contraction of the breast cavity (volumetric cavity change) was also evaluated and used to inform the model. This data was fit to the model by optimizing four mechanobiological parameters: the contractile force of fibroblasts (t_ρ) and myofibroblasts ($t_{\rho,c}$), rate of plastic deformation (τ_{λ^p}), and the saturation of mechanical force by collagen (K_t). These physiologically relevant parameters are not noted in the literature and are found to be dependent on one another. Therefore, we use the machine learning method of the Gaussian Process (GP) to better understand the relationship between these parameters and find the ideal range for each parameter based on the time-dependent cavity contraction profile.

2.2 Methods

2.2.1 Mechanobiological Model

The computational mechanobiological model is a custom solver made through C++ code that has been developed previously to explore cutaneous wounds and the effects of a newly developed collagen dermal replacement scaffold [29]–[31]. Our iteration of the model utilizes a unique generalized breast geometry, created, and meshed in COMSOL (COMSOL Multiphysics, Burlington, MA), that simulates BCS. Specific parameter values from the previous 3D cutaneous wound model have also been modified slightly to be specific to the breast. An overview of the model can be seen below, with a more detailed description available in the following papers [29]–[31]. Corresponding parameter values and descriptions for each equation can also be found in Tables 2.6 and 2.7 in the Appendix.

The fibroblast proliferation and cytokine transport equations can be seen in eqs. (3.7) and (2.2). These equations are interdependent on each other and inform time-dependent changes in both the fibroblast density (ρ) and cytokine concentration (c) throughout the model. For the cavity domain, the fibroblast density is initially at a value of 0 $cells/mm^3$ and steadily increases before reaching a steady-state value of ρ_0= 1000 $cells/mm^3$. This happens through the diffusion of the fibroblasts, as they are guided by the inflammatory response released by the cytokines. The cytokine concentration is initially at a value of $c_0 = 1 \times 10^{-4}$ g/mm^3 in the cavity, as cytokines are released in response to the void. Throughout the wound healing process, the cytokine concentration decays in response to less inflammation due to the ongoing presence of fibroblasts and myofibroblasts. The fibroblast and cytokine source terms are shown in eqs. (3.8) and (3.9).

$$\dot{\rho} = -\nabla \cdot D_\rho \nabla \rho \ - \nabla \cdot D_{\rho,c} \rho \nabla c \ + s_\rho \tag{2.1}$$

$$\dot{c} = -\nabla \cdot D_c \nabla c \ + s_c \tag{2.2}$$

$$s_\rho = \left(p_\rho + p_{\rho,c} \frac{c}{K_{\rho,c} + c} \right) \left(1 - \frac{\rho}{K_{\rho\rho}} \right) \rho - d_\rho \rho \tag{2.3}$$

$$s_c = (p_{c,\rho} c) \left(\frac{\rho}{K_{c,c} + c} \right) - d_c c \tag{2.4}$$

Coupled with both the fibroblast and cytokine density is the collagen (ϕ) deposition (3.15). The production of collagen follows the same timeline as the fibroblast concentration through a similar generation term. The fibroblast and cytokine component in the decay term delays collagen creation during the inflammatory stage, as the cytokine concentration during this period is high. As time progresses, and the cytokine concentration decreases, this decay term decreases as well, allowing for an increase in collagen production.

$$\dot{\phi} = \left(p_\phi + p_{\phi,c} \frac{c}{K_{\phi,c} + c} + p_{\phi_e} H(J^e) \right) \left(\frac{\rho}{K_{\phi,\rho} + \phi} \right) - (d_\phi + c\rho d_{\phi,c})\phi \,. \tag{2.5}$$

For the mechanics of the model, we assume mechanical equilibrium through the balance of linear momentum in the absence of a body force (eq. 2.6). Further, the deformation gradient, which describes local geometry changes, is split into two separate components to capture the elastic and plastic deformation (eq. 3.1).

$$\nabla \cdot \sigma = \mathbf{0} \tag{2.6}$$

$$\mathbf{F} = \mathbf{F}^e \mathbf{F}^p \tag{2.7}$$

The total stress is divided into two components considering active and passive stresses (eq. 3.11). The passive material response is assumed to be hyperelastic through the strain energy function shown in eq. 3.12. The strain energy function accounts for the behavior of the isotropic non-collagenous matrix in the ECM through a neo-Hookean model while also considering the anisotropic mechanical response of the collagen fibers. The active stress is defined through eq. 3.14 and is dependent on fibroblast, cytokine, and collagen density.

$$\sigma = \sigma^{act} + \sigma^{pas} \tag{2.8}$$

$$\Psi = \phi \left(k_0(I_1^{\mathrm{e}} - 3) + \frac{k_1}{2}(J^{\mathrm{e}} - 1)^2 - 2k_0 \log(J^{\mathrm{e}}) \right.$$
$$\left. + \frac{k_f}{2k_2} \exp\left([k_2(\kappa I_1^{\mathrm{e}} + (1 - 3\kappa) I_4^{\mathrm{e}}) - 1]^2 \right) \right) \quad (2.9)$$

$$\sigma^{act} = \rho \left(t_\rho + \frac{t_{\rho,c} c}{K_{t,c} + c} \right) \left(\frac{\phi}{K_t^2 + \phi^2} \right) \hat{\mathbf{A}} \quad (2.10)$$

Heavily dependent on the collagen synthesis rate is the change in plastic deformation shown in eq. 3.16. Plastic deformation occurs independently in the three directions of the orthonormal frame $\mathbf{a}_0, \mathbf{s}_0, \mathbf{n}_0$ ($\alpha = \{a, s, n\}$). With this, plastic deformation only occurs beyond the set threshold of λ^{crit}.

$$\dot{\lambda}_\alpha^p = \dot{\phi}^+ \frac{1}{\tau_{\lambda^p}} \langle \lambda_\alpha^{\mathrm{e}} - \lambda^{crit} \rangle \quad (2.11)$$

2.2.2 Breast Composition and Material Properties

The two major types of tissue that are heterogeneously distributed across the breast are fibroglandular and fat tissue. To accurately model the mechanical field of deformation, the material properties of both tissue types are necessary. Han et al. (2011) performed a patient-specific study across five patients determining the Youngs modulus ratio between fibroglandular and fat tissue along with the Poissons ratio [32]. In assuming adipose was a reference material with $E_{fat} = 10$ kPa, they found that three patients had a fibroglandular:fat tissue Youngs modulus ratio between 2.97 and 4.23 [32]. Further confirmation of these approximations came with a comprehensive study done earlier by Gefen and Dilmoney (2007), where they evaluated multiple studies with a Youngs modulus ratio between 1 and 6.7 [33]–[39]. From this, we estimated for the model that E_{fat}= 10 kPa and $E_{fibroglandular}$= 40 kPa. We are also assuming that breast tissue is a nearly incompressible material, therefore, the Poissons ratio is υ= 0.49.

With the dispersion of the fibroglandular and fat tissue varying patient-to-patient, the models generalized geometry was simplified to make the two tissue types homogeneous. This allowed E_{fat} and $E_{fibroglandular}$ to be combined into one Youngs modulus value based on the percent tissue composition in the breast. Nelson et al. (2008) reported that the average tissue composition for women is approximately 30% fibroglandular tissue and 70% fat tissue [40]. Through the rule of mixtures, the calculated homogeneous breast tissue Youngs modulus was E_{BT}=19 kPa. This value along with the Poissons ratio can further be used to inform parameters k_0 and k_1 in the strain energy function (eq. 3.12). These parameters are the neo-Hookean contribution for linear stiffness and compressibility, which can be calculated using equations for the shear modulus and bulk modulus (eqs. 2.12 and 2.13) [32]. For the average breast composition implemented in the model, k_0= 6.376×10^{-3} MPa and k_1= 0.317 MPa. Table 2.1 shows a summary of possible parameters based on the percent composition of each tissue. Breast composition is classified through BI-RADS, which considers the percentage of fibroglandular tissue in the breast [41].

Table 2.1. Calculated material properties of the generalized breast geometry for different breast compositions.

BI-RADS Classification of Breast Composition	**Frequency of Breast Composition from Nelson et al. (2008) [40]**	**Fibroglandular:Fat Tissue Ratio**	E_{BT} **(kPa)**	k_0 **(MPa)**	k_1 **(MPa)**
Extremely Dense	27.3%	90%:10%	37	1.242×10^{-2}	0.617
		80%:20%	34	1.141×10^{-2}	0.567
Heterogeneously Dense	23.9%	70%:30%	31	1.040×10^{-2}	0.517
		60%:40%	28	9.396×10^{-3}	0.467
		50%:50%	25	8.389×10^{-3}	0.417
Scattered Areas of Fibroglandular Density	44.3%	40%:60%	22	7.383×10^{-3}	0.367
		30%:70%	19	6.378×10^{-3}	0.317
Almost Entirely Fatty	4.5%	20%:80%	16	5.369×10^{-3}	0.267
		10%:90%	13	4.362×10^{-3}	0.217

$$k_0 = \frac{E}{2(1+\upsilon)} \tag{2.12}$$

$$k_1 = \frac{E}{3(1-2\upsilon)} \tag{2.13}$$

2.2.3 Model Geometry

The model implements a generalized breast geometry that is not unique to any patient. Breast and cavity volumes were determined through the evaluation of available clinical data that analyzed the contraction of a breast cavity after whole-breast irradiation. With cavity contraction being an important component in our model, replicating these clinical parameters would ensure the models predictability and accuracy. However, the initial time point of these studies is not directly after surgery, as radiation treatment is often performed weeks later. Since there is limited clinical data that fit our desired time frame from post-surgery to six weeks, the radiation studies were assumed to be a reasonable alternative. Table 2.2 displays a series of results from five clinical radiation studies, which use multiple computerized tomography (CT) scans to predict the breast and cavity volumes across time.

From the collected radiation studies, the Oh et al. (2006) initial geometry parameters were used to represent the models generalized breast geometry. With a breast volume of 774 cm^3 and a tumor cavity volume of 32.1 cm^3, these measurements fit within the broad range seen from the studies in Table 2.2 [42]. Another reason for choosing this specific study was the time between surgery and initial measurements, as an average of 60.9 days is the longest duration out of the evaluated studies [42]. This entails that the initial surgical cavity is farther along in the wound healing process, allowing for better isolation in wound contraction due to only whole-breast irradiation. This relationship was also explored by Oh et al. (2006) and Kim et al. (2008) who found that change in cavity volume across the radiation treatment and time elapsed between surgery to initial measurements showed an inversely proportional trend [42], [43].

The specific location of the cavity was determined through the analysis of several studies characterizing the location of tumors across the breast. These studies classify tumor location based on five specified areas. The central portion is around the area of the nipple, and the remaining region is split into four separate quadrants across the breast, as shown in Figure 2.1. Table 2.3 shows a summary of clinical studies evaluating tumor locations. Across each study, it is reported that tumors are found in the upper outer quadrant approximately 50%

of the time [13], [44]–[47]. Based on these findings, our model assumed the placement of the tumor cavity within the upper outer quadrant of the breast.

Table 2.2. Breast and cavity volume clinical data from clinical radiation studies.

	Oh et al. (2006) [42]	Hurkmans et al. (2009) [48]	Flannery et al. (2009) [49]	Prendergast et al. (2009) [44]	Tersteeg et al. (2009) [50]
Average Breast Volume [range] (cm^3)	774 [596-951]	[487-2736]	1029 [240-3429.1]	1324 [282-3101]	Not Available
Average Initial Cavity Volume [range] (cm^3)	32.1 [25.1-39.2]	40 [14.9-58.4]	38.2 [4.1-363.8]	36.3	78.7 [1.1-236]
Average Final Cavity Volume [range] (cm^3)	25.1 [18.8-31.5]	28, 27, 25 [14.9-58.4]	21.7 [4.7-164.6]	15.8	29.7 [1.3-123.6]
Average % Decrease in Cavity Volume	22.5%	30%, 32.5%, 37.5%	32%	44.6%	62%
Average Time Between Measurements [range] (days)	[28-42]	21, 35, 49	44	49 [35-81.3]	37 [29-74]
Average Time Between Surgery and Initial Measurements [range] (days)	60.9 [20.3-259]	34.5 [20.7-59.1]	31 [4-59]	21	27 [12-74]

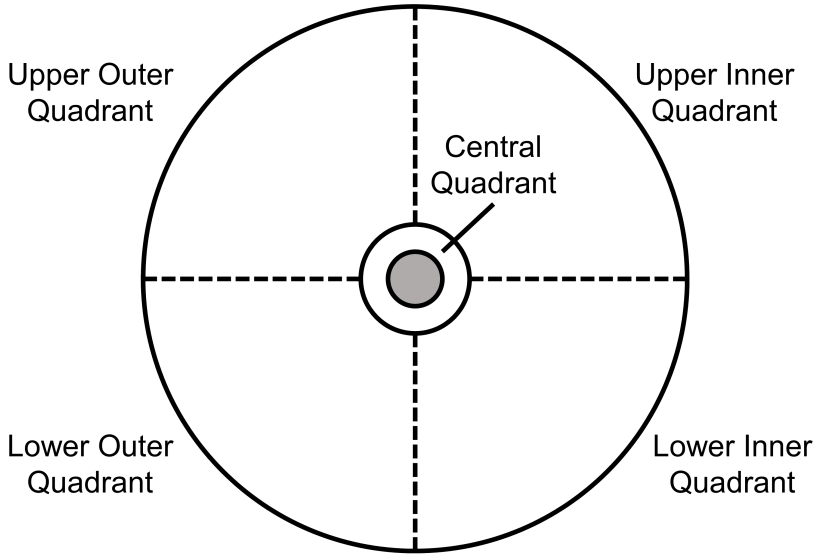

Figure 2.1. Classification of the breast when locating tumors (right breast displayed).

Table 2.3. Clinical results of tumor placement throughout the breast.

	Vos et al. (2018) [13]	Rummel et al. (2015) [45]	Prendergast et al. (2009) [44]	Darbe (2005) [46]	Kroman et al. (2003) [47]
Number of Patients	69	980	36	212,677	35,319
Upper Outer Quadrant	47.8%	51.5%	50.0%	52.5%	50.0%
Upper Inner Quadrant	20.3%	15.6%	25.0%	14.6%	12.9%
Lower Outer Quadrant	18.8%	14.2%	8.0%	9.8%	17.0%
Lower Inner Quadrant	4.3%	8.1%	11.0%	6.4%	6.4%
Central Portion	8.7%	10.5%	6.0%	16.8%	7.3%

These clinical findings were enough to create a final version of the visualized breast geometry, shown in Figure 2.2. The shape of the breast was assumed to be a hemisphere while the cavity was approximated to be a sphere. In addition to the breast domain, a 2 cm thick chest wall is also utilized for the application of the Dirichlet boundary condition.

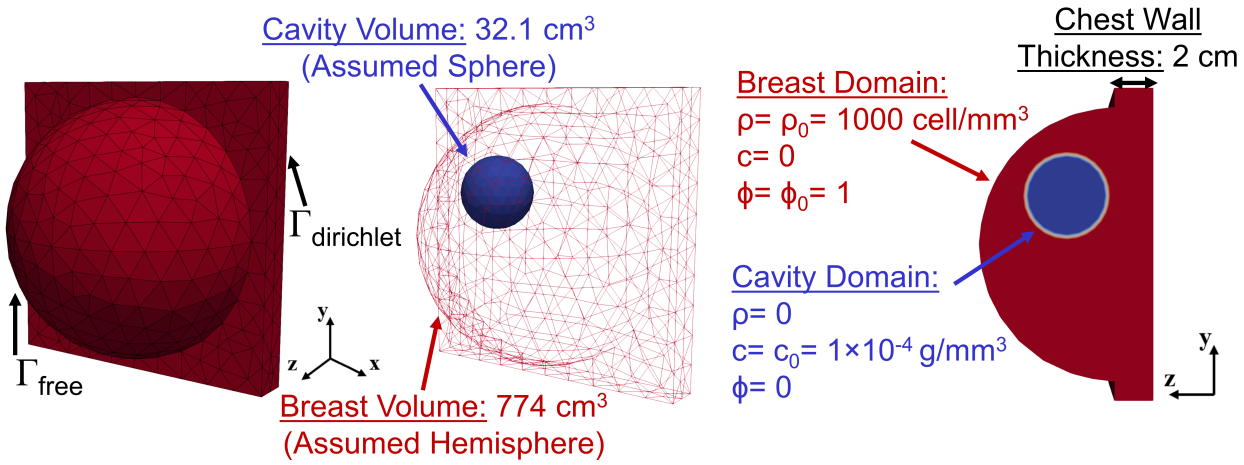

Figure 2.2. Geometry and meshing of the generalized breast geometry showing key geometry features, parameter values, and boundary conditions.

2.2.4 Gaussian Process

The Gaussian Process (GP) is a machine learning method that incorporates past collected data, allowing for the prediction of non-tested parameter sets [51]. In this case, the GP is trained with a curve that tracks the volume of the cavity across time (wound contraction curve), simulated using the coupled mechanobiological model, and visualized in ParaView (ParaView, Clifton Park, NY). The corresponding four parameter values that were used to create each curve were also used as input for the GP. The wound contraction was tracked for six weeks, starting at the initial point of surgery, with 100 training points being taken from each curve throughout the interval. This was used to find the underlying distribution for each training curve, as the distribution updates as new training points are observed. These fittings allow for the creation of a predictive regression line with a corresponding average and variance for any combination of parameter inputs within their respective ranges, shown in Table 2.4 [51].

Table 2.4. Parameter and initial ranges used in the GP.

Parameter	Description	Initial Range
t_ρ (MPa)	Contractile Force of Fibroblasts	$[7.5 \times 10^{-7}, 2 \times 10^{-5}]$
$t_{\rho,c}$ (MPa)	Contractile Force of Myofibroblasts	$[2 \cdot t_\rho, 10 \cdot t_\rho]$
K_t (-)	Saturation of Mechanical Force by Collagen	[0.05, 0.5]
τ_{λ^p} (hr)	Rate of Plastic Deformation	[0.00485, 0.2425]

To assure that we were capturing every aspect of the parameter space for the wound contraction training curves, we used the Latin hypercube sampling algorithm (LHS). This is a method of random sampling that effectively distributes samples across the parameter space, which can be efficient in reducing the number of runs necessary to capture the parameter space. LHS was performed four separate times, with 25 parameter sets per run. For all sampling done with LHS, only t_ρ, τ_{λ^p}, and K_t were varied in their respective ranges, while $t_{\rho,c}$ was constant at $10 \cdot t_\rho$. We then varied $t_{\rho,c}$ at the two values of $2 \cdot t_\rho$ and $5 \cdot t_\rho$, while keeping all other parameter values constant. Values of t_ρ, τ_{λ^p}, and K_t were selected based on existing combinations found through the prior LHS sampling. This method produced 25 more training curves. In combining the two methods, a total of 97 training curves were simulated, as all simulated curves that failed to converge before reaching the six-week time frame were not used. Following the proper training of the GP, predictive regression lines can be created confidently through the selection of any parameter combination within the ranges.

The morphology of the contraction curves was further analyzed to see if they fit within the targeted solution based on results from Oh et al. (2006). This study found the average decrease in the cavity volume to be 22.5%, as shown in Table 2.2 [42]. As we modeled our breast geometry from this study, a similar contraction level should be shown in the targeted predictive curves. Due to this, we have the target steady-state wound contraction between a 20% and 25% cavity volume decrease. Another trend that is shown across each contraction curve is the contraction dip. The contraction dip is calculated as the difference between the steady-state contraction value and the maximum contraction level across the six

Table 2.5. Target parameter value ranges found using the GP.

Parameter	Description	Initial Range	Target Range
t_ρ (MPa)	Contractile Force of Fibroblasts	$[7.5 \times 10^{-7}, 2 \times 10^{-5}]$	$[3.5 \times 10^{-6}, 2 \times 10^{-5}]$
$t_{\rho,c}$ (MPa)	Contractile Force of Myofibroblasts	$[2 \cdot t_\rho, 10 \cdot t_\rho]$	$[2 \cdot t_\rho, 10 \cdot t_\rho]$
K_t (-)	Saturation of Mechanical Force by Collagen	[0.05, 0.5]	[0.05, 0.243]
τ_{λ^p} (hr)	Rate of Plastic Deformation	[0.00485, 0.2425]	[0.00485, 0.07275]

weeks. From collected clinical data and literature, a severe contraction dip has never been reported throughout the healing of a breast cavity [12], [48]. Therefore, our targeted wound contraction dip is any value less than 15%. The steady-state wound contraction and the contraction dip were recorded for every predictive wound contraction curve. Any predicted curve that had a predictive variance above 0.001 was deemed untrained and excluded from the results.

2.3 Results and Discussion

2.3.1 Target Parameter Range

The desired parameter values for the outputted predictive curves were found by linearly spacing each of the four parameters in intervals of eight, creating the combination to allow for 4096 predictive wound contraction curves. When categorizing these curves based on steady-state contraction and the contraction dip, only 24 curves fit within the target steady-state contraction values (0.75-0.80) and the target contraction dip values ($\leq$0.15). The four varying parameter values were captured for each target curve and were used to narrow down the initial parameter range (Table 2.4). The found target parameter range can be seen in Table 2.5. In comparison to the initial range that was used for the GP, it can be seen that to fit the target morphology, t_ρ must not have a value in the lower end of the initial range, τ_{λ^p} and K_t must be on the lower end of their respective ranges, and $t_{\rho,c}$ was found to have the exact same target range as the initial set range.

2.3.2 Parameter Relationship

To better define the relationships between the parameters, the predictive contraction curves, and their corresponding morphology was displayed in two-dimensional (2D) contour plots. This was done by linearly spacing only two parameters in intervals of 50, creating the combination to allow for 2500 predictive wound contraction curves. The two unvaried parameters were kept constant at a value that fits well within the target range from Table 2.5.

Figure 2.3 displays the morphology contour plots when varying K_t and t_ρ. It was found that both cavity contraction and contraction dip increase as t_ρ increases. With this, increasing K_t resulted in decreasing cavity contraction and contraction dip. These opposite effects result in high cavity contraction and contraction dip for high t_ρ and low K_t values. Furthermore, large decreases in both cavity contraction and contraction dip were more prone to occur for lower values of K_t. This evidence suggested that neither parameter is dominant over the other, as both play pivotal roles in characterizing the steady-state contraction and contraction dip.

The contour plots varying K_t and $t_{\rho,c}$ are shown in Figure 2.4. The relationship with K_t and the corresponding morphology is very similar to the contour shown in Figure 2.3. With this, $t_{\rho,c}$ is found to have similar tendencies as t_ρ. This means as $t_{\rho,c}$ increases, both the cavity contraction and the contraction dip increase. The difference comes with the influence of $t_{\rho,c}$, as contours seem to be more horizontal compared to Figure 4. This shows that the influence $t_{\rho,c}$ has on the morphology is not as significant as t_ρ.

The next contour plot evaluated was the relationship between τ_{λ^p} and t_ρ, shown in Figure 2.5 With the impact of t_ρ on the morphology already analyzed, the focus of this contour is on the trends shown with τ_{λ^p} and its impact on the morphology. The contour plots show a vertical relationship between the parameters, meaning that t_ρ has a clearly greater influence compared to τ_{λ^p}. In these contours, as τ_{λ^p} increases, the cavity contraction decreases slightly, and the contraction dip increases.

To better show the influence that τ_{λ^p} has, Figure 2.6 displays the contour plots between τ_{λ^p} and $t_{\rho,c}$. The steady-state contraction contour displays a clear positive slope while the

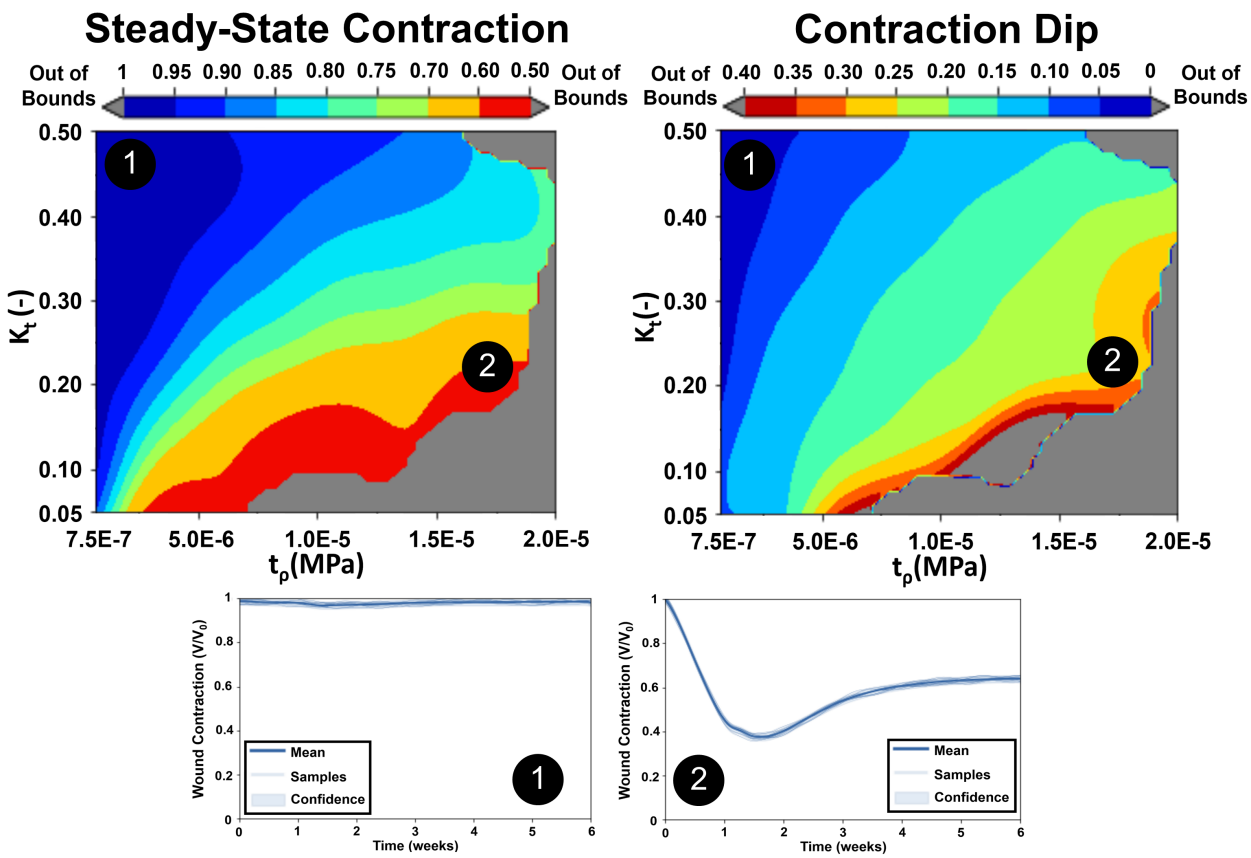

Figure 2.3. Contour plots and corresponding reference wound contraction curves varying the force of fibroblasts (t_ρ) and the saturation of mechanical force by collagen (K_t) with constants τ_{λ^p}= 0.0388 and $t_{\rho,c}$=10 $\cdot$ t_ρ.

contraction dip shows a negative sloping contour, supporting the fact that both τ_{λ^p} and $t_{\rho,c}$ have a very similar influence on the curve morphology. One interesting coupling shown is that the contraction dip is also more sensitive to changes in $t_{\rho,c}$ for higher values of τ_{λ^p}.

2.4 Conclusion

We were able to successfully calibrate the computational model using human clinical data from the literature and effectively simulate the breast healing response following BCS. Furthermore, by using the GP to gain insight into the uninformed parameter space and identify target morphology for the wound contract process, we successfully narrowed down the range of each parameter while obtaining a deeper understanding of the parameter relationships.

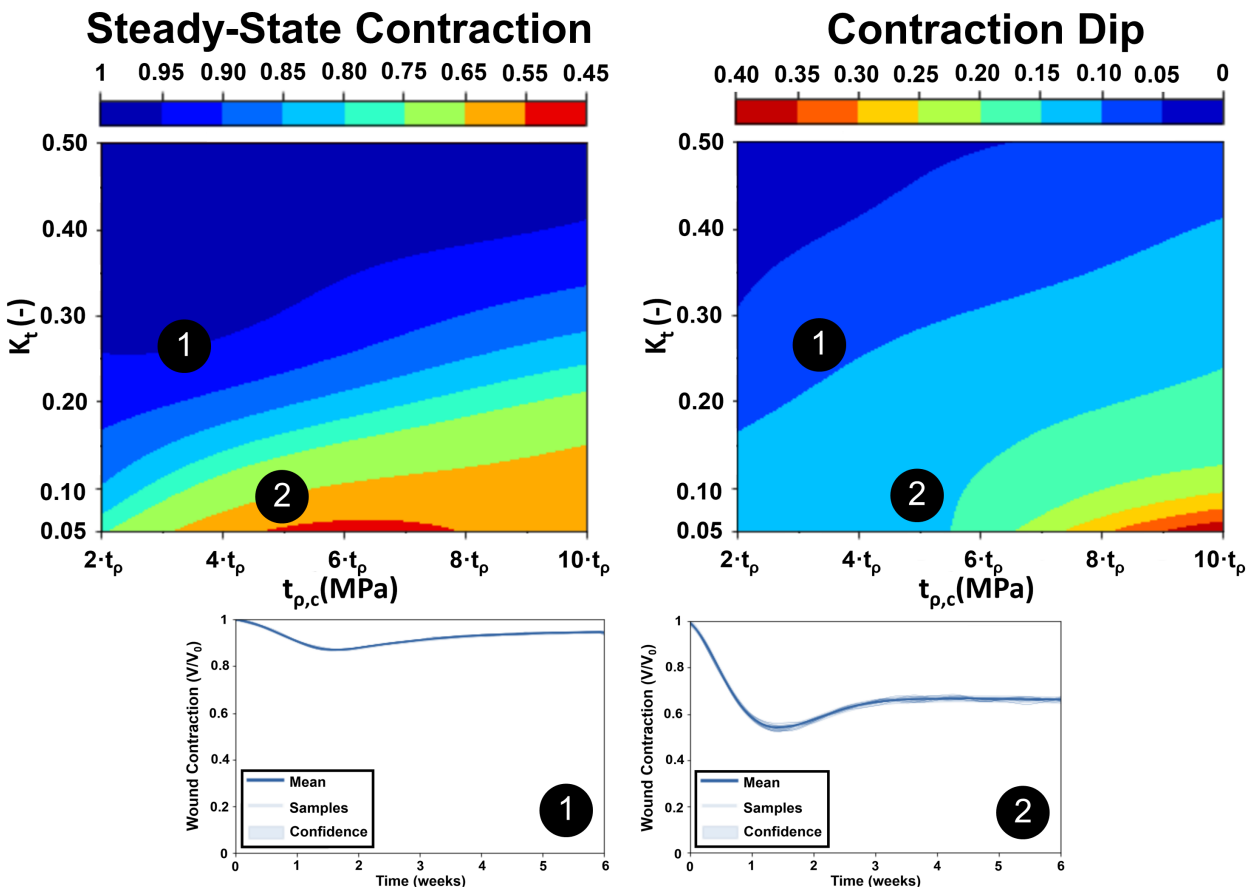

Figure 2.4. Contour plots and corresponding reference wound contraction curves varying the force of myofibroblasts ($t_{\rho,c}$) and the saturation of mechanical force by collagen (K_t) with constants t_ρ=6.25 $\times$ 10^{-6} and τ_{λ^p}= 0.0388.

Increasing the contractile force of the fibroblasts and myofibroblasts (t_ρ and $t_{\rho,c}$) was found to increase cavity contraction and contraction dip while the saturation of mechanical force by collagen (K_t) had the opposite effect. Finally, increasing the rate of plastic deformation (τ_{λ^p}) decreased the cavity contraction and increased the contraction dip. With this, t_ρ and K_t were found to be very influential on cavity contraction when compared to $t_{\rho,c}$, and τ_{λ^p}. The clear definitions of the parameters showed that machine learning processes, like the GP, provide a useful and computationally inexpensive method for prioritizing and defining mechanobiological healing parameters for use in the computational BCS model. Future efforts of the model will focus on the further calibration of the model based on available

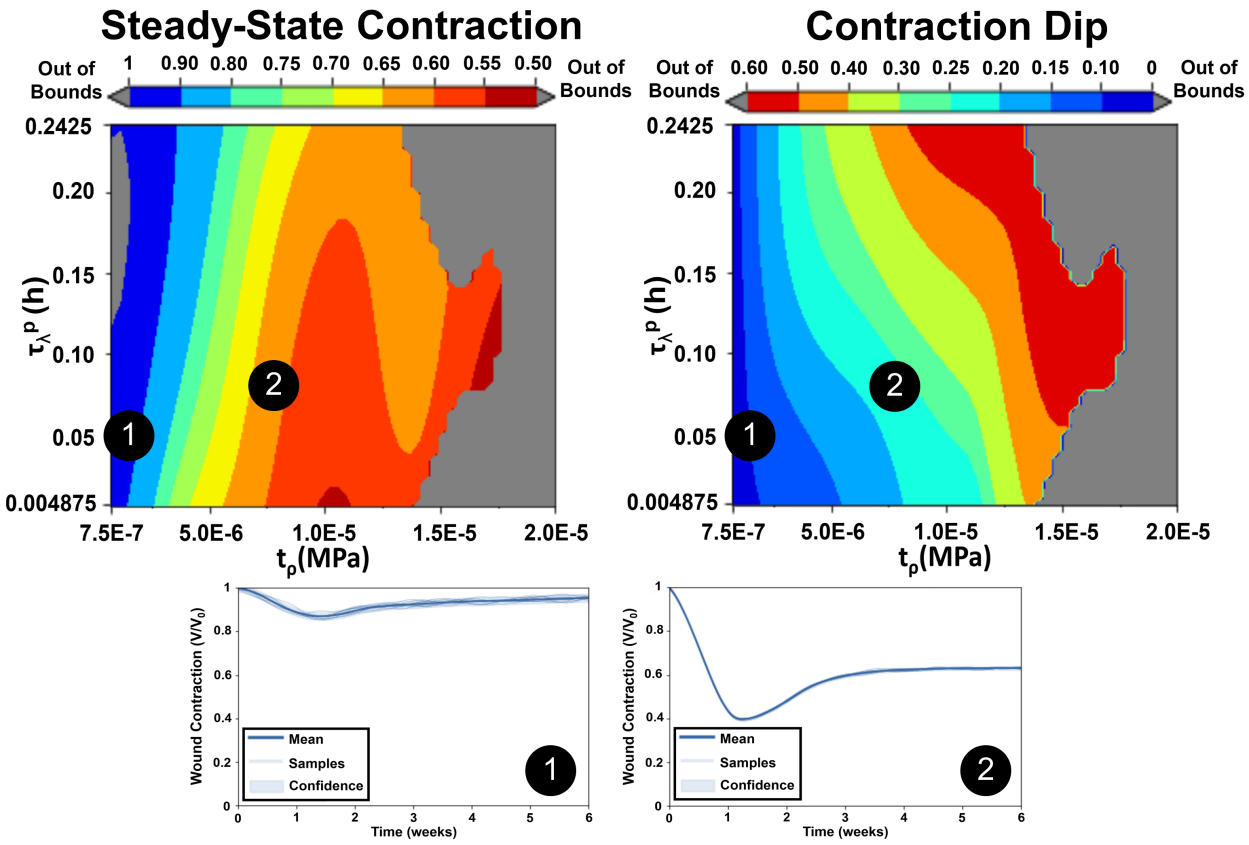

Figure 2.5. Contour plots and corresponding reference wound contraction curves varying the force of fibroblasts (t_ρ) and the rate of plastic deformation (τ_{λ^p}) with constants K_t=0.15 and $t_{\rho,c}$=$10 \cdot t_\rho$.

patient-specific BCS data in the presence and absence of radiation therapy and preclinical animal data evaluating new breast restoration (e.g. soft tissue filler) therapies.

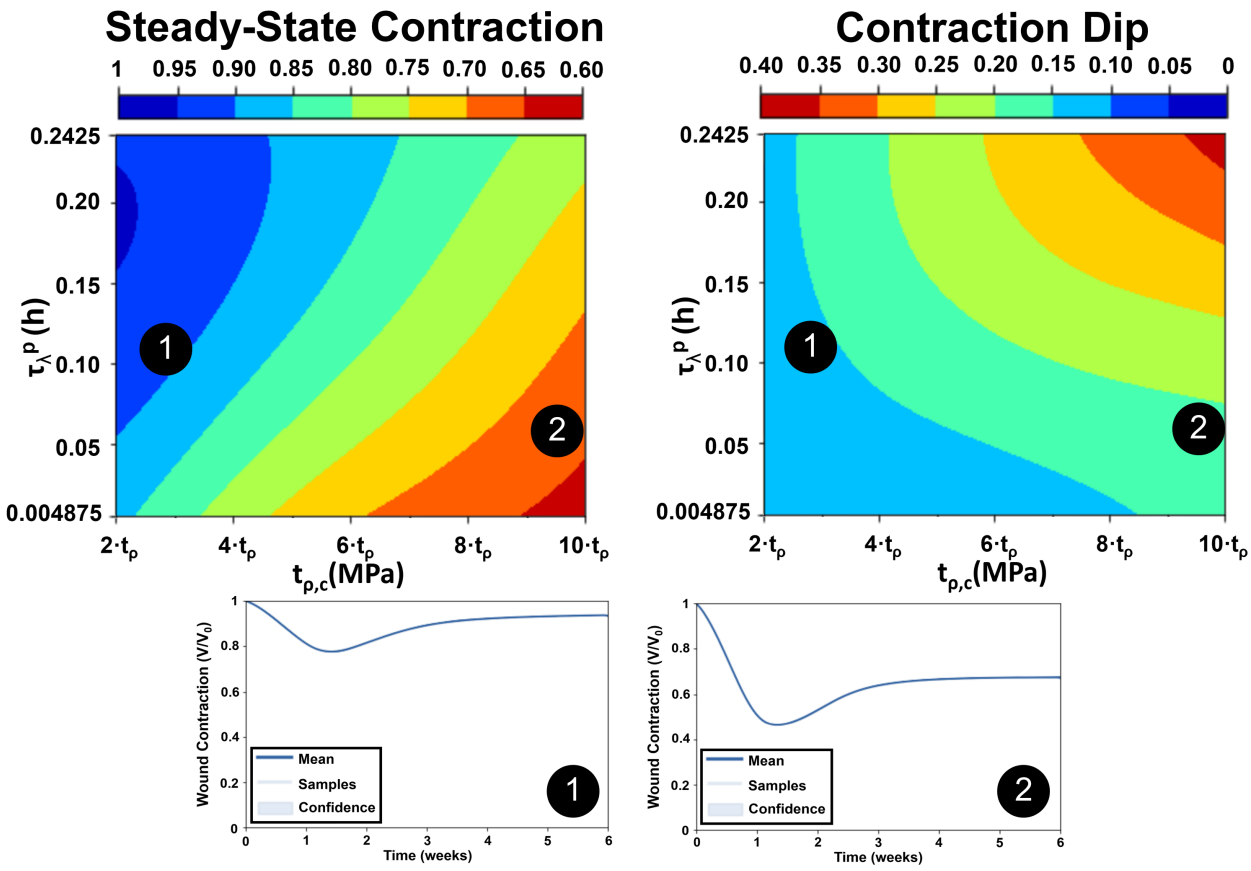

Figure 2.6. Contour plots and corresponding reference wound contraction curves varying the force of myofibroblasts ($t_{\rho,c}$) and the rate of plastic deformation (τ_{λ^p}) with constants t_ρ=6.25 $\times$ 10^{-6} and K_t=0.15.

2.5 Appendix

Table 2.6. Parameters for the biochemical model. Parameters listed as estimated were selected in this work or modified from our previous wound healing models [30], [31].

Parameter	Description	Value	Reference
D_ρ $[mm^2/hr]$	Cell Diffusion Coefficient	0.0833	[52], [53]
$D_{\rho,c}$ $[mm^3/mol/hr]$	Chemotaxis Coefficient	1.66×10^{-4}	[30], [54]
D_c $[mm^2/hr]$	Cytokine Diffusion Coefficient	0.01208	[54]–[56]
p_ρ $[1/hr]$	Fibroblast Proliferation	0.017	[52]
$p_{\rho,c}$ $[1/hr]$	Cytokine-Increased Fibroblast Proliferation	$p_\rho/2$	[31]
$K_{\rho,c}$ [-]	Proliferation Saturation due to Cytokine	1×10^{-5}	[30]
$p_{\rho,\mathrm{e}}$ $[1/hr]$	Mechanoregulation of Fibroblast Proliferation	$p_\rho/2$	[31]
$K_{\rho,\rho}$ [-]	Fibroblast Division Saturation	$10,000$	[52]
d_ρ $[1/hr]$	Fibroblast Death Rate	$p_\rho(1-\rho_{phys}/K_{\rho\rho})$	[52]
$p_{c,\rho}$ $[1/hr]$	Fibroblast Secretion of Cytokine	9×10^{-19}	[30]
$p_{c,\mathrm{e}}$ $[1/hr]$	Mechanoregulation of Cytokine	3×10^{-18}	[30]
$K_{c,c}$ $[mol/mm^3]$	Cytokine Saturation	1	[30]
d_c $[1/hr]$	Cytokine Death Rate	0.01	Estimated
ρ_0 $[cells/mm^3]$	Nominal Fibroblast Density	1000	[57], [58]
c_0 $[g/mm^3]$	Initial Cytokine Concentration Inside Cavity	1×10^{-4}	[30]

Table 2.7. Parameters for the fully coupled mechanobiological model. Parameters listed as estimated were selected in this work or modified from our previous wound healing model [30], [31].

Parameter	Description	Value	Reference
k_0 $[MPa]$	Linear Stiffness	6.375×10^{-3}	Estimated
k_1 $[MPa]$	Compressibility	0.317	Estimated
k_f $[MPa]$	Fiber Stiffness	0.015	[59]
k_2 [-]	Nonlinear Stiffening	0.048	[59]
γ_e [-]	Mechanoregulation of Fibroblast Proliferation	5	[30]
ϑ_e [-]	Fibroblast Division Saturation	2	[30], [60]
$K_{t,c}$ $[-]$	Traction Saturation due to Cytokine	1×10^{-5}	[30]
$K_{\phi,c}$ $[-]$	Collagen Production Saturation due to Cytokine	1×10^{-4}	[30]
p_{ϕ_e} $[1/hr]$	Collagen Production Activated by Stretch	p_ϕ	[30]
$K_{\phi,\rho}$ $[-]$	Collagen Production Saturation due to Collagen Fraction	$(\rho_0 * p_\phi)/d_\phi - 1$	[30]
d_ϕ $[1/hr]$	Collagen Degradation	9.7×10^{-4}	[61]
$d_{\phi,c}$ $[1/hr]$	Collagen Degradation Activated by Cytokine	4.85×10^{-4}	[61]
τ_ω $[hr]$	Time Constant for Reorientation	$10/(K_{\phi,\rho}+1)$	[30]
τ_κ $[hr]$	Time Constant for Dispersion	$1/(K_{\phi,\rho}+1)$	[30]
γ_κ [-]	Shape of Dispersion Rate Curve	2	[30]

3. COMPUTATIONAL MECHANOBIOLOGY MODEL TO ASSIST WITH PREDICTION OF HEALING AND COSMETIC OUTCOMES FOLLOWING BREAST-CONSERVING SURGERY

3.1 Introduction

Breast cancer is the most common cancer in women, with approximately 287,850 women in the United States alone being diagnosed in 2022 [1]. Increased awareness, early detection with frequent screenings, and expanded treatment options have improved breast cancer survival rates over time, with recent 5-year survival rates reported to be 90.6% [2]. Given these high survival rates, increased focus has been placed on long-term outcomes and patient quality of life after treatment. At present, the lowest rates of cancer recurrence are associated with surgical treatment options [62], [63]. As a result, breast cancer patients and their surgeons are often faced with choosing between breast-conserving surgery (BCS; otherwise known as lumpectomy) or mastectomy (removal of the whole breast), a decision-making process that is challenging, multi-faceted, and stressful. In recent years, BCS has replaced mastectomy as the preferred standard of care for early-stage breast cancer, since BCS has similar or improved survival rates and decreased risk of complications compared to mastectomy [5]–[8]. With the goal of preserving healthy breast tissue and breast appearance, BCS involves the removal of the cancerous tissue along with a small margin of healthy tissue. As shown in Figure 3.1, the resulting tissue cavity undergoes a wound healing process that ultimately leads to variable levels of tissue contraction, scar tissue formation, and breast deformation (i.e., cosmetic defects, including dents, distortions, and asymmetries between breasts). The prognosis of a good cosmetic outcome typically weighs heavily on physician and patient selection of BCS over mastectomy, since good aesthetics has been associated with improved patient psychological recovery and quality of life [9], [10]. However, the complex nature of the tissue repair process as well as significant variations in patient-specific characteristics, make it extremely challenging, if not impossible, for surgeons to predict post-surgical healing, oncologic, and cosmetic outcomes. The inability to predict healing and breast deformation outcomes stems

from the complex interplay between tissue mechanics, inflammatory-mediated biochemical and cellular signaling, and (myo)fibroblast mechanobiology during the tissue repair process. Therefore, there is a need for an improved mechanistic understanding of the multi-scale breast healing process along with definition of critical patient-specific characteristics that affect BCS outcomes. With this knowledge, surgeons and their patients can better develop individualized treatment plans that lead to decreased post-surgical complications, decreased surgical procedures (e.g., re-excision, revision, and/or reconstruction), and improved patient satisfaction and quality of life [5].

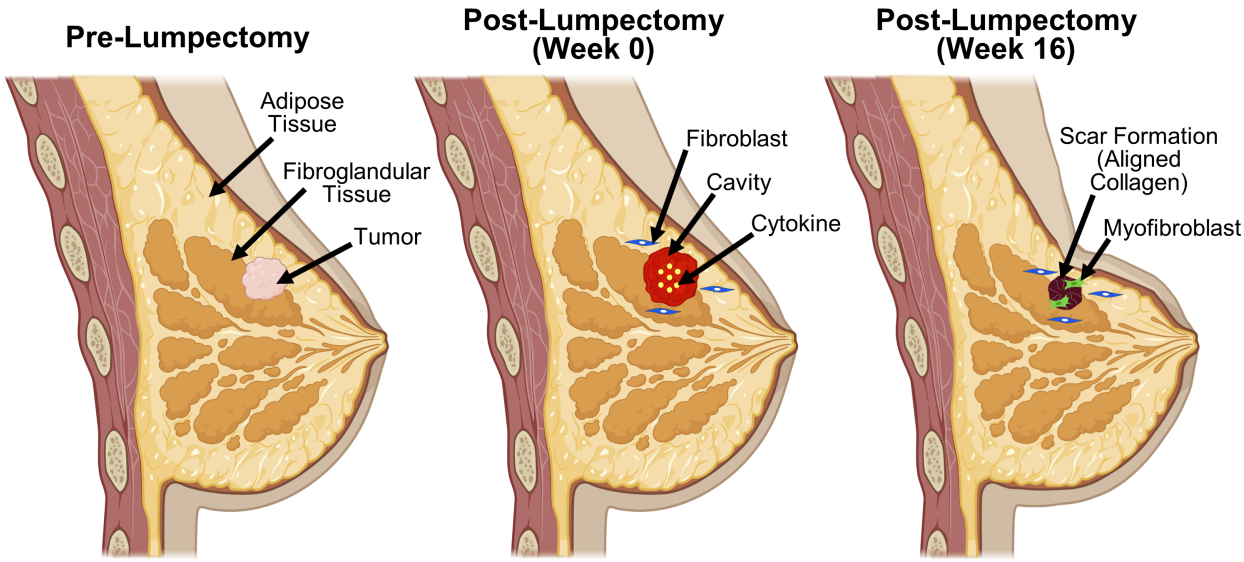

Figure 3.1. Schematic of cavity healing process following removal of breast tumor by lumpectomy. Tumor is excised along with a small margin of surrounding healthy tissue, forming a fluid-filled cavity. The surgical void undergoes the normal wound healing process, with hemostasis and inflammatory phases resulting in the creation of a cytokine gradient within the cavity. In turn, cytokines induce fibroblast proliferation, resulting in collagen deposition and scar formation through collagen fiber alignment. Fibroblast differentiation into myofibroblasts further promotes contraction of the cavity and surrounding tissue, which may contribute to breast deformities.

Given that few objective criteria and limited surgical decision-making tools exist, pre-operative predictions of healing, oncologic, and breast cosmetic outcomes remain largely dependent on a surgeons past training and experience [64]. BCS surgical planning has been an evolving area over the past several years, as physicians work to further inform and stan-

dardize the process. In 2014 and 2016, the Society of Surgical Oncology (SSO), the American Society of Radiation Oncology (ASTRO), and the American Society of Clinical Oncology (ASCO), published consensus guidelines on adequate surgical margins when treating various types and stages of breast cancer with BCS and whole breast irradiation [3], [65]. Additionally, surgical decision trees have been developed based on correlative analyses of human BCS patient data, including tumor-to-breast volume percentage (TBVP), tumor location, breast cosmetic outcome assessments, and quality of life surveys [13], [23], [24]. While these decision-making tools provide recommendations on treatment thresholds (i.e., when to treat a patient with BCS versus mastectomy) based on tumor size and location, they have yet to receive widespread adoption. Feedback regarding patient satisfaction and quality of life, as provided through $BREAST-Q^{TM}$ questionnaires and other patient surveys, has informed surgeons of other patient-specific factors affecting BCS outcomes [66]. More specifically, results from multivariable clinical analyses revealed that increased excised breast volume percentage (EBVP), decreased breast density (as measured by BI-RADS rankings), increased patient age and body mass index, breast irradiation, and concomitant adjuvant chemotherapy and radiotherapy often negatively influence surgical outcomes and patient satisfaction. [14], [15], [67]–[69]. In summary, since patient-specific characteristics are intertwined and significantly affect post-lumpectomy healing and cosmetic outcomes, there is a need for a predictive tool to better understand the mechanistic interplay between these contributing factors.

Computational models provide useful tools that can assist with informing, predicting, and simulating wound healing outcomes, including surgical wounds associated with BCS. In general, wound healing can be modeled as four, overlapping phases: hemostasis, inflammation, proliferation (or granulation), and remodeling [29]. To date, numerous numerical-based approaches have been developed to describe healing of superficial skin layers, including the epidermis and/or the dermis [70]. However, unlike skin wounds, which have an air-tissue interface, BCS yields a fully-enclosed cavity or void that resides relatively deep within the breast tissue. Healing of these deep, soft tissue wounds begins immediately following cavity creation, with blood clots (hematomas) and/or serous fluid (seromas) often filling the void [12]. The fibrin matrix, with its limited persistence and mechanical integrity, serves as a

provisional scaffold, allowing local tissue contraction while promoting inflammation and cellularization. Platelet degranulation and cytokine secretion by inflammatory cells contributes to the formation of a cytokine gradient within the cavity, which, in turn, promotes fibroblast proliferation and migration into the wound space. Fibroblast proliferation, migration, and differentiation into myofibroblasts are further guided by fibrillar collagen deposition, and scaffold reorganization/contraction, ultimately creating a dense, stiff scar tissue within the contracted cavity. Scar tissue formation and remodeling over time are perhaps the most unpredictable aspects of BCS, since it is known to contribute to pain, breast deformations, and altered breast consistency, all of which negatively affect women emotionally and psychologically [17].

In recent years, computational models have also been developed for the purpose of predicting specific surgical outcomes following BCS. For example, Garbey and collaborators proposed a two-dimensional (2D) model to predict time-dependent changes in breast shape following lumpectomy [26], [27]. This model was calibrated using 1D MRI (magnetic resonance imaging) profiles obtained for a single patient [27]. Vavourakis and collaborators developed a 3D finite element model to predict breast deformation following BCS. Model validation was performed using a combination MRI and optical surface scans for 4 patients obtained before and 6 to 12 months after BCS [28]. Unfortunately, computational models developed to date lack a thorough calibration against experimental or clinical breast healing data. Additionally, present-day models do not fully capture the complex couplings between cellular mechanobiological activity, extracellular matrix (ECM) deposition and remodeling, and cavity and breast plastic deformation over time. Descriptions of collagen deposition, granulation tissue formation, and remodeling are especially important to capture, as the breast cavity and surrounding tissue will undergo large deformations and permanent contracture.

In this paper, we work to address this gap in wound mechanobiology modeling following BCS by presenting a theoretical and computational framework calibrated against animal model and clinical data. Here, we adapt our previously developed experimentally-calibrated model of dermal wounds that accounts for couplings between cellular mechanobiological activity, plastic deformations, and tissue remodeling [31], [71]. This informed 3D finite element

model is then used to inform a machine learning surrogate model in order to evaluate the effect of specific mechanobiological parameters and patient-specific characteristics on healing and breast deformation outcomes. The proposed model has the potential to assist surgeons in creating an individualized treatment plan for patients that better predict oncologic, healing, and cosmetic outcomes.

3.2 Methods

The computational breast mechanobiological model represents a custom finite element solver implemented in C++. The link to the code repository is provided at the end of the manuscript. The software builds upon and extends our previous dermal wound healing models [29]–[31]. An overview of the model and associated adaptations is discussed below, with more detailed descriptions available in our previous work [30], [31]. Detailed parameter descriptions and values are included in Tables 3.3 and 3.4 in the Supplementary Material.

3.2.1 Geometry

We considered the two breast lumpectomy geometries shown in Figure 3.2. Both geometries were created and meshed in COMSOL (COMSOL Multiphysics, Burlington, MA). One geometry (Fig. 3.2A) corresponded to a generalized porcine breast based on a preclinical porcine lumpectomy study by Puls et al. (2021) [12]. Available ultrasound and explant images were used to estimate the dimensions of the ellipsoidal cavity ($a = b = 1.5$ cm, $c = 0.6$ cm) along with a cavity depth of 1.15 cm. The cavity represented approximately one-quarter of the total breast volume (quadrantectomy). The breast was assigned the shape of a half-ellipsoid ($a = b = 2.32$ cm, $c = 2$ cm), enclosed within a rectangular region (15 cm by 15 cm by 2 cm) of connective tissue.

An idealized human breast lumpectomy geometry was developed based on average breast and cavity sizes reported in a human clinical study by Prendergast et al. (2009) [44]. As shown in Figure 3.2B, the breast was modeled as a hemisphere with a radius of 8.58 cm and the cavity was modeled as a sphere with a radius of 3.02 cm. Since the upper outer quadrant is reported to be the most prevalent tumor location [13], [44]–[47], this cavity location was

assumed in the model. Breast cavity contraction over a four-week period following BCS, as quantified by Prendergast and co-workers, was also used for model calibration.

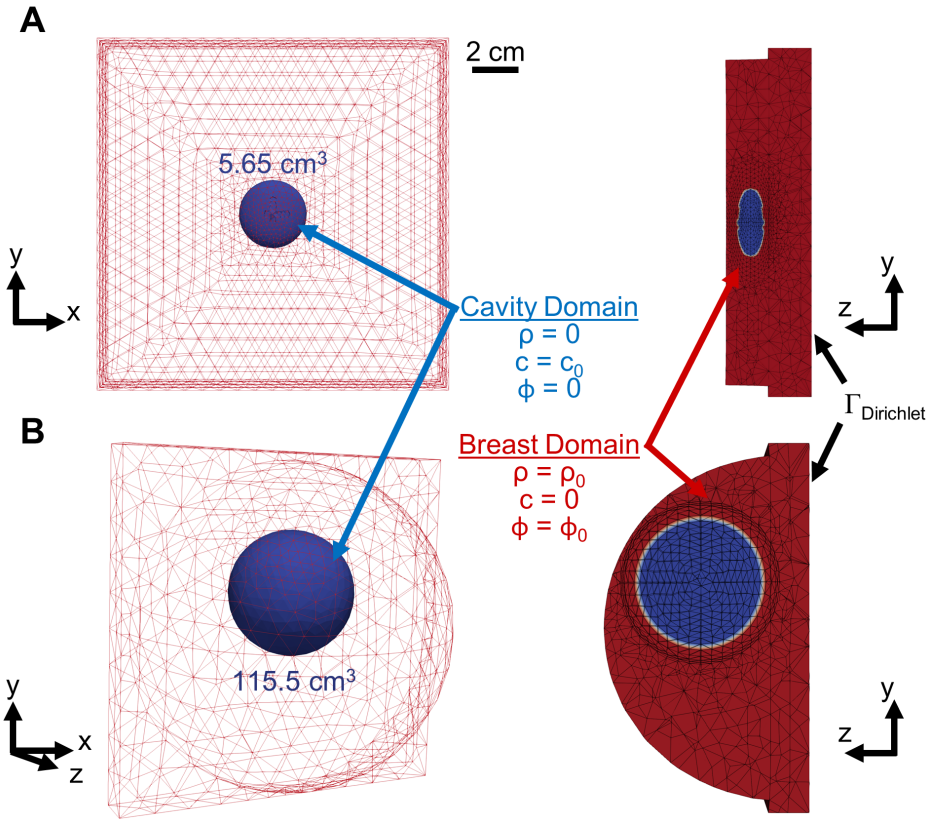

Figure 3.2. Meshing, initial conditions, and boundary conditions for the (A) porcine and (B) human breast geometries. For the porcine geometry, the breast was assumed to be a half-ellipsoid (22.60 cm^3) and the cavity was assumed to be an ellipsoid (5.65 cm^3), with both dimensions based on a quadrantectomy. The tissue external to the breast was modeled as connective tissue. For the human geometry, the breast was assumed to be a hemisphere with a volume of 1,324 cm^3 and the cavity was assumed to be a sphere with a volume of 115.5 cm^3. The Dirichlet boundary condition was applied to the interior surface of the 2-cm thick chest wall while the exterior surface of the breast was a free boundary.

3.2.2 Kinematics

The reference geometries displayed in Figure 3.2 are described with material coordinates $\mathbf{X} \in \mathcal{B}_0 \subset \mathbb{R}^3$. Through the deformation mapping φ, the time-dependent configuration,

$\mathcal{B}_t$, is obtained as $\mathbf{x} = \varphi(\mathbf{X}, t)$. The fibroblast density, cytokine concentration, and collagen density are $\rho(\mathbf{x}, t), c(\mathbf{x}, t), \phi(\mathbf{x}, t)$, respectively. The collagen matrix is further defined through the fiber dispersion $\kappa(\mathbf{x}, t)$ and the preferred fiber orientation $\mathbf{a}_0(\mathbf{x}, t)$. The deformation gradient $\mathbf{F} = \partial\mathbf{x}/\partial\mathbf{X}$, which describes local geometry changes, can be split into two separate components capturing the elastic and plastic deformation

$$\mathbf{F} = \mathbf{F}^{\mathrm{e}}\mathbf{F}^{p}\,. \tag{3.1}$$

Furthermore, the plastic deformation tensor is described with three scalar fields

$$\mathbf{F}^{p} = \lambda_a^p \mathbf{a}_0 \otimes \mathbf{a}_0 + \lambda_s^p \mathbf{s}_0 \otimes \mathbf{s}_0 + \lambda_n^p \mathbf{n}_0 \otimes \mathbf{n}_0\,, \tag{3.2}$$

where vectors $\mathbf{a}_0, \mathbf{s}_0, \mathbf{n}_0$ form an orthonormal basis around the preferred fiber orientation $\mathbf{a}_0$.

3.2.3 Constitutive and Balance Equations

The change in the fields introduced in the previous section are classified into three categories. The *biological* fields ρ, c satisfy mass balance in the form of reaction-diffusion partial differential equations (PDEs). The *microstructural* fields $\phi, \lambda_a^p, \lambda_s^p, \lambda_n^p, \kappa, \mathbf{a}_0$ do not have a diffusion component and their change is local. The microstructural fields are directly coupled to the *mechanical* field of deformation φ, which satisfies momentum balance.

Biochemical Model

The fibroblast and cytokine concentrations satisfy standard advection-diffusion transport equations

$$\dot{\rho} = \nabla \cdot Q_\rho + s_\rho \tag{3.3}$$

$$\dot{c} = \nabla \cdot Q_c + s_c\,, \tag{3.4}$$

where Q_ρ, Q_c are flux terms akin to Fickian diffusion

$$Q_\rho = -D_\rho(\phi, c)\nabla\rho \tag{3.5}$$

$$Q_c = -D_c\nabla c\,. \tag{3.6}$$

While the diffusion coefficient for the cytokine is assumed constant, cell diffusion (migration) is affected by both cytokine and collagen concentrations,

$$D_\rho = d_{\rho,\phi}\frac{v_\rho^2(\phi)}{6} + d_{\rho,c}\frac{c}{K_{\rho,c}+c} + d_{\rho,0} \tag{3.7}$$

with parameters $d_{\rho,\phi}, d_{\rho,c}, d_{\rho,0}$. The first term in eq.(3.7) reflects the direct dependence of fibroblast speed on collagen density, while the second and third terms are related to the baseline diffusion coefficient for cells in native tissue and their change in diffusivity with c considering Michaelis Menten kinetics. The initial profile for $v_\rho(\phi)$ was estimated through available in-vivo wound healing data [12], [72]. The expression was then modified through a parameter Δ, which skews the collagen concentration associated with maximum fibroblast speed. Additional information about $v_\rho(\phi)$ and Δ can be found in Figure 3.11 in the Supplementary Material.

The source terms s_ρ, s_c are

$$s_\rho = \left(p_\rho + p_{\rho,c}\frac{c}{K_{\rho,c}+c} + p_{\rho,\mathrm{e}}H(J^\mathrm{e})\right)\left(1-\frac{\rho}{K_{\rho\rho}}\right)\rho - d_\rho\rho \tag{3.8}$$

$$s_c = (p_{c,\rho}c + p_{c,\mathrm{e}}H(J^\mathrm{e}))\left(\frac{\rho}{K_{c,c}+c}\right) - d_c c\,, \tag{3.9}$$

with parameters $p_\rho, p_{\rho,c}, K_{\rho,c}, p_{\rho,\mathrm{e}}, K_{\rho\rho}, d_\rho$ for the fibroblast source, and $p_{c,\rho}, p_{c,\mathrm{e}}, K_{c,c}, d_c$ for the cytokine. The values of all parameters are listed in Table S1 in the Supplementary Material.

Note that most dependencies of the biological fields are on other biological fields, but some couplings exist in the microstructural and mechanical fields. For instance, cell migration in eq. (3.7) depends on the microstructural field ϕ through v_ρ defined in the Supple-

mentary Material. The biological fields are also coupled to the mechanical field through the mechanosensing logistic function, $H(J^{\mathrm{e}})$ in eqs. 3.8 and 3.9 described below.

Mechanical Model

Balance of linear momentum in the absence of body force is reduced to the standard equation

$$\nabla \cdot \sigma = \mathbf{0}\,. \tag{3.10}$$

However, here the total stress is split into two separate components for active and passive stress contributions

$$\sigma = \sigma^{act} + \sigma^{pas}\,. \tag{3.11}$$

The active stress is described in the following section devoted to the mechanobiological couplings. In this section, we focus on the passive part. The passive material response is assumed hyperelastic with the strain energy function

$$\Psi = \phi \left(k_0(I_1^{\mathrm{e}} - 3) + \frac{k_1}{2}(J^{\mathrm{e}} - 1)^2 - 2k_0 \log(J^{\mathrm{e}}) \right. \\ \left. + \frac{k_f}{2k_2} \exp\left([k_2(\kappa I_1^{\mathrm{e}} + (1 - 3\kappa) I_4^{\mathrm{e}}) - 1]^2 \right) \right) \tag{3.12}$$

parameterized by k_0, k_1, k_2, k_f. It is also a function of the microstructure fields ϕ, κ, and of the elastic invariants of the deformation $I_1^{\mathrm{e}}, J^{\mathrm{e}}, I_4^{\mathrm{e}}$. Note that only the elastic part of the deformation contributes to the strain energy. Based on the split eq.(3.1), the elastic volume change is $J^{\mathrm{e}} = \det(\mathbf{F}^{\mathrm{e}})$, the first isotropic invariant is the trace of the elastic right Cauchy Green tensor $I_1^{\mathrm{e}} = \mathrm{tr}(\mathbf{F}^{\mathrm{e}\top}\mathbf{F}^{\mathrm{e}})$, and the fourth invariant describes the deformation in the preferred fiber direction $I_4^{\mathrm{e}} = \mathbf{a}_0 \cdot \mathbf{F}^{\mathrm{e}\top}\mathbf{F}^{\mathrm{e}}\mathbf{a}_0 = \mathbf{a} \cdot \mathbf{a}$, with $\mathbf{a}$ representing the deformed fiber orientation.

The parameters k_0 and k_1, which correspond to a neo-Hookean contribution, were determined using the rule of mixtures assuming that human and porcine breast tissue, on average,

is composed of 70% adipose tissue and 30% fibroglandular tissue [40]. Han et al. (2011) and several other studies were used to inform material properties for adipose and fibroglandular tissue, as we estimated Young's modulus for adipose and fibroglandular tissue to be 10 kPa and 40 kPa, respectively [32]–[39], [73]. The parameter k_f denotes collagen fiber stiffness for the scar tissue [59]. Mechanical parameter descriptions and values are included in Table 3.4 in the Supplementary Material.

Mechanobiological Coupling

As mentioned before, the biological fields are linked to the mechanical deformation by the logistic function $H(J^{\mathrm{e}})$ in eqs. 3.8 and 3.9. This function encodes a mechanosensing activation as the deformation deviates from homeostasis

$$H(J^{\mathrm{e}}) = \frac{1}{1+\exp(-\gamma_{\mathrm{e}}(J^{\mathrm{e}}-\vartheta^{\mathrm{e}}))}\,, \tag{3.13}$$

with parameters $\gamma_{\mathrm{e}}, \vartheta_{\mathrm{e}}$. Another coupling that appeared already in eq. (3.11) is the active stress, which is defined as

$$\sigma^{act} = \rho\left(t_\rho + \frac{t_{\rho,c}c}{K_{t,c}+c}\right)\left(\frac{\phi}{K_t^2+\phi^2}\right)\hat{\mathbf{A}} \tag{3.14}$$

which depends on the fibroblast density ρ, the cytokine c, the collagen density ϕ, and the preferred fiber orientation through the structure tensor $\hat{\mathbf{A}} = \mathbf{A}/\mathrm{tr}(\mathbf{A})$, $\mathbf{A} = \mathbf{I}+(1-3\kappa)\mathbf{a}\otimes\mathbf{a}$. The parameters of the active stress eq. (3.14) are $t_\rho, t_{\rho,c}, K_t, K_{t,c}$, with parameter descriptions and values provided in Table 3.4 in the Supplementary Material.

The other mechanobiological coupling that was introduced earlier is the fibroblast migration dependence on collagen density in a non-monotonic fashion through v_ρ in eq. (3.7) [31].

The last set of equations needed to close the model are the rate equations for the microstructural fields. Collagen deposition is encoded by

$$\dot{\phi} = \left(p_\phi + p_{\phi,c}\frac{c}{K_{\phi,c}+c} + p_{\phi_{\mathrm{e}}}H(J^{\mathrm{e}})\right)\left(\frac{\rho}{K_{\phi,\rho}+\phi}\right) - (d_\phi + c\rho d_{\phi,c})\phi\,, \tag{3.15}$$

with dependence on both cell density and cytokine concentration. Descriptions and values of parameters $p_\phi, p_{\phi,c}, K_{\phi,c}, p_{\phi_e}, K_{\phi,\rho}, d_\phi, d_{\phi,c}$) in eq. (3.15) are included in Table 3.4 in the Supplementary Material. The change in plastic deformation occurs independently in all three directions

$$\dot{\lambda}_\alpha^p = \dot{\phi}^+ \frac{1}{\tau_{\lambda^p}} \langle \lambda_\alpha^e - \lambda^{crit} \rangle \tag{3.16}$$

where $\alpha = \{a, s, n\}$ are the three directions of the orthonormal frame $\mathbf{a}_0, \mathbf{s}_0, \mathbf{n}_0$. The term $\dot{\phi}^+$ in eq. (3.16) is the positive part of the rate of change of collagen (i.e., the new collagen deposition rate), which contributes to deformation plastification. The Macaulay brackets $\langle \bullet \rangle$ specify that plastic deformation only occurs beyond some threshold deformation λ^{crit}.

Lastly, the change in preferred collagen fiber orientation and dispersion are based on the eigenvalues of the deformation

$$\dot{\mathbf{a}}_0 = \lambda_1 \left(\frac{2\pi \dot{\phi}^+}{\tau_\omega} \right) (\mathbf{I} - \mathbf{a}_0 \otimes \mathbf{a}_0) \mathbf{e}_1 \,, \tag{3.17}$$

where $\lambda_1, \mathbf{e}_1$ are the largest eigenvalue and corresponding eigenvector, respectively. Eq. (3.17) essentially reorients the principal fiber direction to the direction of maximum principal stretch, with time constant τ_ω dependent on collagen deposition $\dot{\phi}^+$. The fiber dispersion change

$$\dot{\kappa} = \frac{\dot{\phi}^+}{\tau_\kappa} \left(\frac{1}{3} \frac{\lambda_2^{\gamma_\kappa}}{\lambda_1^{\gamma_\kappa}} - \kappa \right) \tag{3.18}$$

depends on the ratio of the first two eigenvalues with a power law parameterized by γ_κ and the time constant τ_κ.

3.2.4 Experimental Data

Time-dependent changes in fibroblast and collagen densities were informed by histopathological data from the porcine lumpectomy study [12]. Hematoxylin and eosin (H&E) stained cross-sections of breast explants were analyzed 1 week, 4 weeks, and 16 weeks following lumpectomy and compared to normal porcine breast tissue (Fig. 3.3). An image of each

cross-section was post-processed in Aperio ImageScope (Leica Biosystems, Vista, CA) and 25 individual regions (500 x 500 μm^2) spanning the cavity domain were extracted. These regions were further processed in ImageJ (National Institutes of Health, Bethesda, MD), where multiple color balance filters were applied to quantify the number fibroblasts, red blood cells (RBCs), and immune cells per region. Fibroblast number per area was used to calculate fibroblast volume density, assuming a tissue section thickness of 4 μm. Additional details of this image analysis process are provided in the Supplementary Material. The H&E stained cross-sections were also used to determine collagen density by correlating collagen density with the intensity of eosin-stained collagen fibers. Eosin intensity for a region of interest was determined using ImageJ and normalized to connective tissue values within adjacent healthy breast tissue values. When calculating normalized collagen densities, an average breast composition of 70% adipose tissue and 30% fibroglandular tissue was assumed [40].

Temporal changes in cytokine concentration were informed by prior human clinical studies that evaluated cytokine levels in seroma fluid, which commonly fills the breast void following surgery. Seroma fluid is known to be composed of cytokines that impact the inflammation and proliferation phases of healing [16]. It has also been reported that seromas formed following BCS resolve within approximately 4 weeks [74]. Based on this, it was assumed that cytokine levels decayed exponentially over approximately a 4-week time period.

3.2.5 Model Calibration Using Gaussian Processes

The finite element model defined in previous sections is computationally expensive and impractical for tasks such as model calibration or sensitivity analysis. Therefore, to calibrate the model against experimental porcine data and human clinical data, we leveraged Gaussian process (GP) surrogates [51]. The methodology for GP model calibration is illustrated in Figure 3.4. Calibration was performed with two separate GPs. First, a submodel consisting only of the biological fields ρ, c and the microstructural field ϕ was isolated out of the complete set of equations with the goal of fitting the porcine histology data (i.e., fibroblast and collagen densities). A second GP was constructed for the fully coupled mechanobiological model. This two-stage approach was used to i) inform biological parameters that could, in

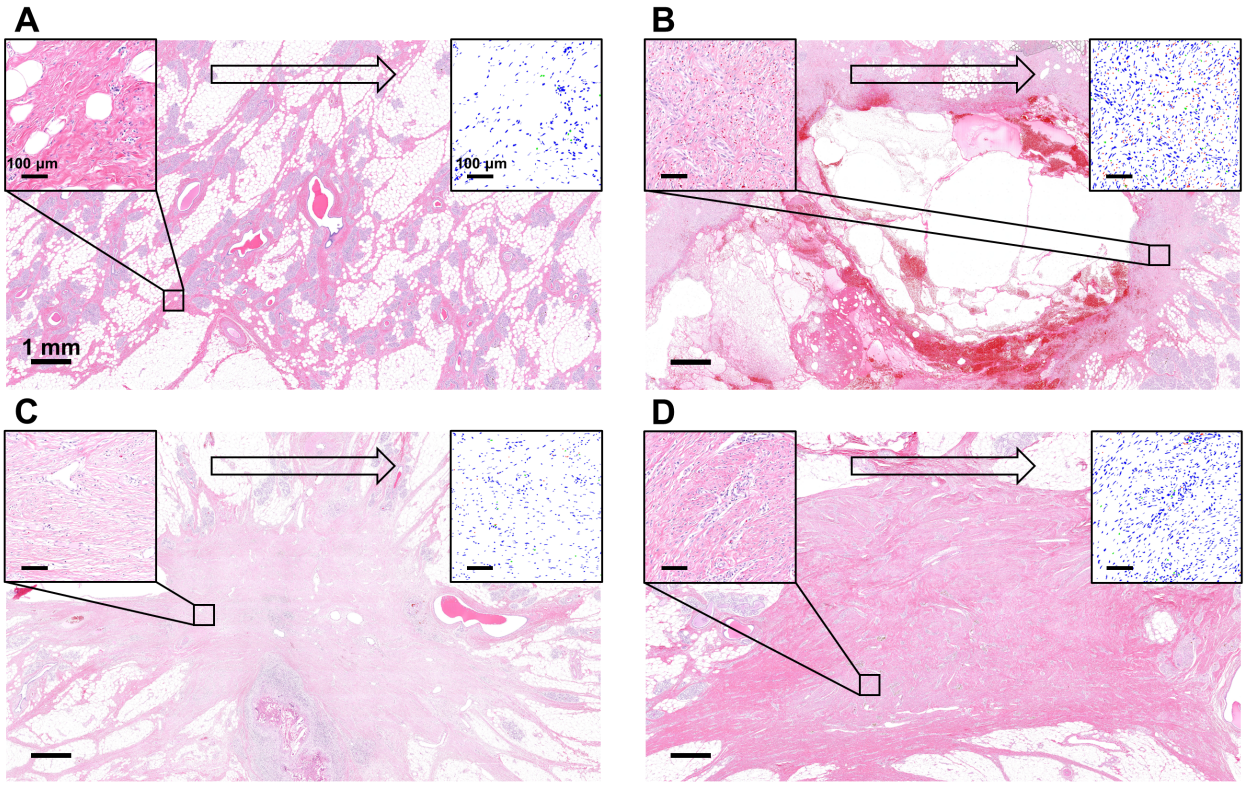

Figure 3.3. Overview of histological image analysis process used to quantify fibroblast and collagen densities within (A) normal porcine breast tissue and porcine breast tissue undergoing progressive healing at (B) 1 week, (C) 4 weeks, and (D) 16 weeks following simulated lumpectomy (quadrantectomy). Individual regions (500 x 500 μm^2) of H&E-stained cross-sections (top left inset) were processed using a particle analyzer (top right inset) for identification and enumeration of fibroblasts (blue), RBCs (red), and immune cells (green). Collagen density was determined by normalizing regional eosin intensity values for connective tissue within healing breasts to eosin intensity in normal breast connective tissue.

turn, be compared with other computational models lacking mechanobiological couplings, and ii) calibrate the mechanobiological coupling terms, for which limited prior information exists.

For the first GP surrogate, 5 parameters $\Theta_b = \{p_{\rho,c}, d_{\rho,\phi}, \Delta, p_\phi, p_{\phi,c}\}$ were sampled from the ranges reported in Table 3.1 using Latin Hypercube Sampling (LHS). All other parameters affecting the submodel $\{\rho, c, \phi\}$ were assigned values from literature or calculated in order

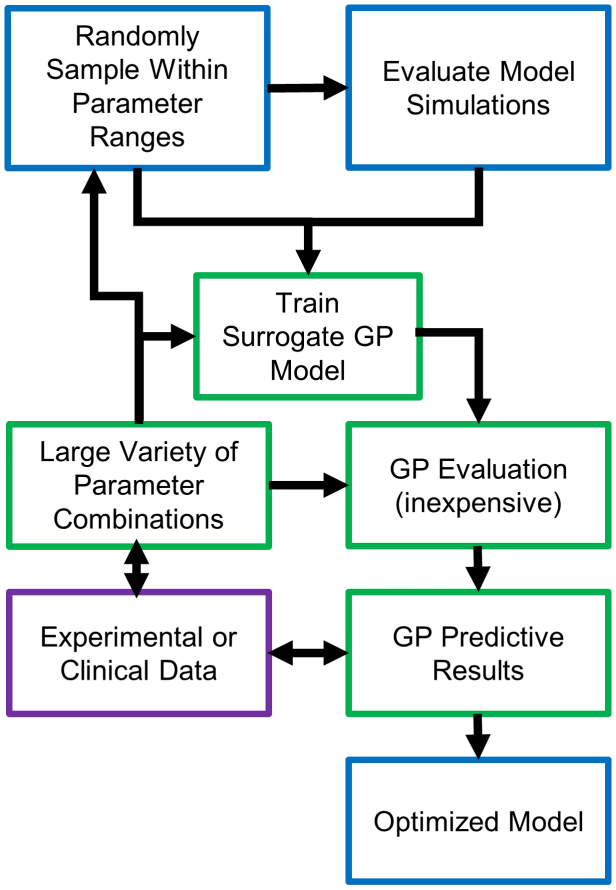

Figure 3.4. GP methodology used to identify optimum biochemical and mechanobiological parameters that best fit porcine lumpectomy histology results and human clinical contraction data. The computational model was run several times, sampling across the entire parameter space to train the GP. Once well-trained, the GP was then used to evaluate a large number of parameter combinations spanning the entire parameter space. By comparing GP generated simulations to experimental and clinical data through RMSE, specific model parameters were optimized.

to satisfy a physiological steady state. In other words, the 5 parameters Θ_b were identified as the adjustable parameters for model calibration. To train the GP, 100 different parameter combinations of Θ_b were generated and applied to the finite element submodel, with fibroblast and collagen density values at the center of the cavity $\rho_C(\mathbf{t}), \phi_C(\mathbf{t})$ representing model outcomes of interest. A total of 196 time steps were extracted from the simulation, covering the time $t \in [0, 16]$ weeks. Following calibration, the GP model was used for minimization

Table 3.1. Biochemical and mechanobiological parameters with established initial ranges that were evaluated and optimized using the biochemical or mechanobiological GP.

Parameter	Description	Range	Optimized Value
Biochemical GP Parameters (Θ_b)			
$p_{\rho,c}$ [1/hr]	Cytokine-Increased Proliferation	[0.0092641, 0.04632]	0.015314
$d_{\rho,\phi}$ [-]	Fibroblast Diffusion Scaling Constant	[62.6793, 12472.9067]	1582.3
Δ [-]	Skewness of Fibroblast Speed $v_\rho(\phi)$	[0, 1]	0
p_ϕ [1/hr]	Collagen Production	$[3.633 \times 10^{-9}, 3.633 \times 10^{-7}]$	1.4×10^{-8}
$p_{\phi,c}$ [1/hr]	Collagen Production Activated by Cytokine	$[3.633 \times 10^{-9}, 3.633 \times 10^{-7}]$	7.0×10^{-8}
Mechanobiological GP Parameters (Θ_m)			
t_ρ [MPa]	Contractile Force of Fibroblasts	$[9.08244 \times 10^{-8}, 5.44947 \times 10^{-7}]$	2.33548×10^{-7}
$t_{\rho,c}$ [MPa]	Contractile Force of Myofibroblasts	$[1 \cdot t_\rho, 5 \cdot t_\rho]$	$3.28571 \cdot t_\rho$
K_t [-]	Saturation of Mechanical Force by Collagen	[0.1, 0.5]	0.2
τ_{λ^p} [1/hr]	Rate of Plastic Deformation	[0.00485, 0.2425]	0.05

of root mean square error (RMSE) by comparing GP predictions for $\hat{\rho}_C(\Theta_b, t)$, $\hat{\phi}_C(\Theta_b, t)$ against porcine histopathological data. After minimization, regions of the parameter space Θ_b with lower RMSE and higher predicted variance were used to select new Θ_b parameter combinations to further train the GP model. Subsequent RMSE minimization with the GP model yielded the optimal parameter values Θ_b.

After calibration of the $\{\rho, c, \phi\}$-submodel, a similar approach was performed to calibrate the mechanobiological parameters $\Theta_m = \{t_\rho, t_{\rho,c}, K_t, \tau_{\lambda^p}\}$. For the second GP model, a total of 100 simulations were run after LHS sampling of Θ_m within the specified ranges in Table 3.1. The trained GP was used to minimize the RMSE with respect to the cavity contraction data from the human clinical study [44]. As described previously, initial minimization was followed by subsequent finite element model parameter evaluations and training of the GP model.

3.3 Results

3.3.1 Pathophysiologic Findings Through Porcine Histology Analysis

Analysis of breast histological cross-sections from a longitudinal porcine lumpectomy study informed fibroblast and collagen densities within the breast cavity at 1, 4, and 16 weeks after surgery. Table 3.2 summarizes values for each post-surgical time point compared

Table 3.2. Fibroblast and collagen densities (mean ± SD) quantified from histological cross-sections of normal, healthy porcine breast tissue and explanted breast tissue at 1 week, 4 weeks, and 16 weeks following lumpectomy. Post-surgical values represent the cavity center.

Time Point	**Fibroblast Density (Mean ± SD)** $[cells/mm^3]$	**Collagen Density (Mean ± SD)** $[\phi/\phi_0]$
Healthy Tissue	55,051 ± 15,527	1 ± 0
1 Week Post-Surgry	0 ± 0	0 ± 0
4 Weeks Post-Surgery	377,504 ± 94,279	1.35 ± 0.25
16 Weeks Post-Surgery	215,893 ± 45,150	2.33 ± 0.35

to healthy breast tissue. Given that hematomas or seromas were observed grossly and histologically 1 week following lumpectomy (Fig. 3.3B), fibroblast and collagen densities were assumed to be zero for this time point. By 4 weeks, fibrovascular scar tissue was evident within the contracted cavity (Fig. 3.3C), with fibroblast and collagen density values roughly 7 and 1.3 times healthy breast tissue values, respectively. By 16 weeks, the fibrous scar tissue increased in collagen density (approximately 2.3 times healthy breast tissue values), appearing as differentially oriented swirls of parallel-aligned fibers (Fig. 3.3D). Although fibroblast density decreased between 4 and 16 week time points, values remained high at roughly 4 times those for healthy breast tissue.

3.3.2 Calibration of the $\{\rho, c, \phi\}$ submodel

Fibroblast and collagen density values reported in Table 3.2 were successfully fit to the $\{\rho, c, \phi\}$ submodel by optimizing the (Θ_b). Predicted fibroblast and collagen density values fell within experimentally-determined standard deviation ranges for all time points (Fig. 3.5). Finite element simulations for the optimized submodel are shown in Figure 3.5, illustrating spatiotemporal changes in fibroblast density, collagen density, and cytokine concentration.

Fibroblast and collagen densities within the cavity center were roughly zero at week 1 of the simulation (Fig. 3.5), successfully modeling hematoma and/or seroma formation and the lack of fibroblast infiltration observed histologically (Fig. 3.3B). Contour plots showed

modest increases in fibroblast and collagen density, respectively, at the cavity-tissue interface (Fig. 3.5), which also matched histological findings (Fig. 3.3B). Fibroblast density increased sharply between weeks 1 and 4 (Fig. 3.5), effectively simulating fibroblast proliferation and migration. An increase in collagen density followed thereafter (Fig. 3.5), which is consistent with progressive collagen deposition by fibroblasts during the proliferation phase of healing. As shown in Figure 3.5, simulation results reached a maximum fibroblast density of 3.95×10^5 $cells/mm^3$ at roughly 4.5 weeks, after which time fibroblast density steadily declined to match histological outcomes. As fibroblast number declined between 4 and 16 weeks, the rate of collagen deposition declined, with collagen density values plateauing within experimentally measured ranges (Fig. 3.5). Simulated cytokine concentration within the cavity started at the maximum nominal value and showed a rapid decay over the first four weeks (Fig. 3.5). Such results are consistent with events and phases of wound healing as reported in the literature [74], [75].

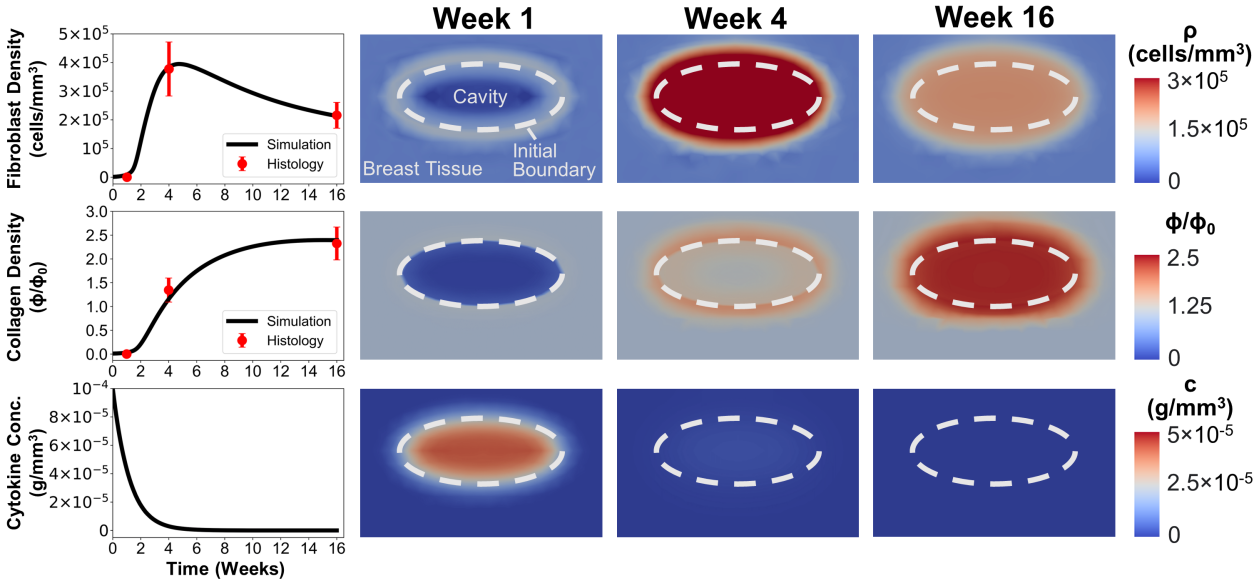

Figure 3.5. Simulation results of the $\{\rho, c, \phi\}$ submodel using optimized parameters Θ_B. Plots display time-dependent changes in fibroblast density, collagen density, and cytokine concentration at the cavity center as determined from simulations and histology. Corresponding contour plots from breast cavity healing simulations are shown for weeks 1, 4, and 16.

3.3.3 Calibration of the Fully Coupled Mechanobiological Model

Human breast cavity contraction data estimated from Prendergast et al. (2009) was fit with the coupled mechanobiological model by optimizing mechanobiological parameters (Θ_m) listed in Table 3.1. Results from the calibrated finite element simulation, including cavity contraction, permanent deformation, and breast surface deformation, are displayed in Figure 3.6. Consistent with human data, the simulated post-surgical breast cavity contracted to approximately 66.49% of its original cavity volume within 1 week. The cavity volume continued to decrease, contracting to 20.90% of its original volume in just 16 days following surgery. By 4 weeks, the cavity showed a modest increase in volume to reach 31.43% of the excised volume. The overall shape of the contraction curve was similar to porcine lumpectomy study findings as well as cavity contraction in human patients following BCS and whole-breast irradiation [12], [48].

Permanent deformation (J^p) was also visible across the cavity domain and surrounding tissue, leading to breast surface deformations (Fig. 3.6B). At the time of tumor removal (t = 0 week), no change in tissue volume is observed across the entire geometry ($J^p = 1$). Immediately thereafter, permanent contracture ($J^p < 1$) becomes prevalent at the tissue-cavity interface, with $J^p = 0.85$ for this region at the 1-week time point. This permanent deformation contributed to a modest surface asymmetry in the upper outer quadrant breast (Fig. 3.6B). By week 4, severe permanent contracture ($J^p = 0.3$) was observed within the cavity while tissue surrounding the cavity was experiencing tensional forces ($J^p > 1$) directed perpendicular to the cavity surface. Such observations are consistent with tissue repair and scar formation, as newly deposited collagen fibers within the cavity are contracted and reoriented by fibroblasts and myofibroblasts and the surrounding tissue ECM is drawn in tension [31], [71]. This permanent contracture contributed to an obvious breast surface deformity adjacent to the cavity (Fig. 3.6B).

3.3.4 Mechanobiological Parameter Sensitivity Analysis

A major goal associated with the calibration of our detailed mechanistic model of breast healing after BCS is to better define key parameters and relationships that influence healing

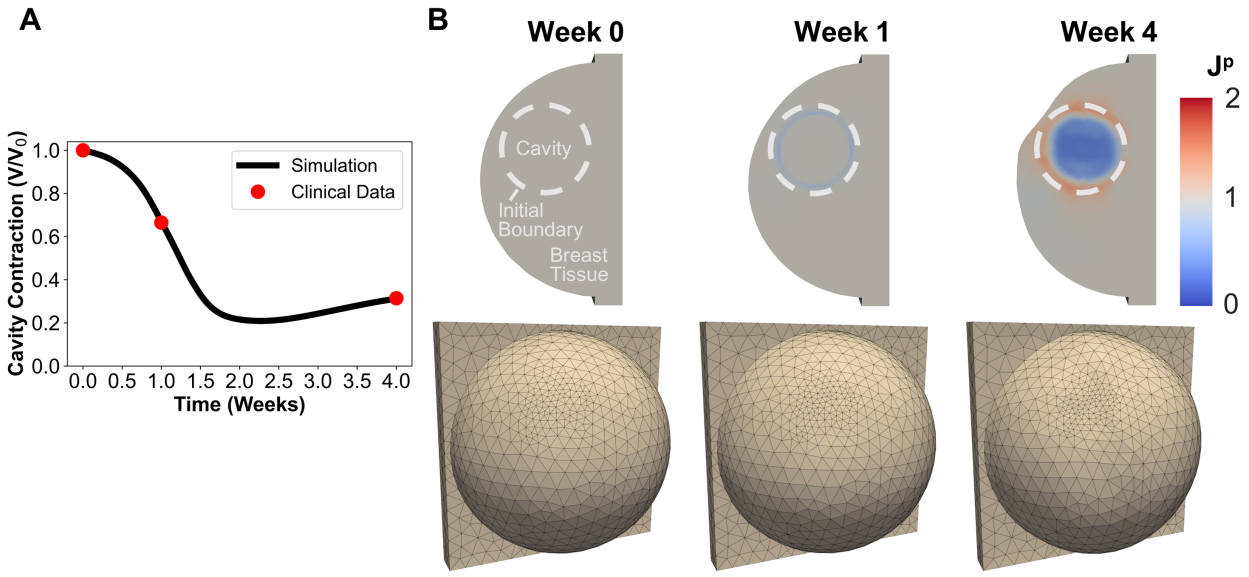

Figure 3.6. Mechanobiological model outcomes using optimized parameters informed by the mechanobiological GP. (A) Simulated post-surgical cavity contraction over time compared to clinical data. (B) Contour plots displaying time-dependent changes in permanent tissue deformation for simulated breast cavity healing (top) and associated breast surface deformation (bottom).

and cosmetic outcomes. In particular, mechanobiological model calibration, as described in previous sections, allowed optimization of parameters Θ_m for which there is little direct experimental or clinical information. An important next step was to explore the sensitivity of model predictions with respect to these parameters. To analyze Θ_m parameter effects, 2500 predictive cavity contraction curves were generated with the calibrated GP by sampling Θ_m values within ranges reported in Table 3.1. The normalized cavity volume at week 4 (V_4/V_0) was probed, with Figure 3.7A-D showing four 2D contour plots where the force of fibroblasts (t_ρ), force of myofibroblasts ($t_{\rho,c}$), saturation of mechanical force by collagen (K_t), and rate of plastic deformation (τ_{λ^p}) were varied.

As shown in Figure 3.7A, cavity contraction was highly dependent on the fibroblast force t_ρ, with increasing force leading to larger contraction. Although K_t had a less pronounced effect, increasing the saturation of mechanical force by collagen was found to decrease cavity contraction. Due to this inverse relationship, low K_t values and high t_ρ values produced the

largest contractions, with the cavities contracting to less than 25% of their initial volume by week 4. Cavity contraction also increased with increasing myofibroblast force $t_{\rho,c}$; however, an interesting coupling was identified between K_t and $t_{\rho,c}$ (Fig. 3.7B). Evaluation of t_ρ and K_t pairings (Fig. 3.7A) clearly showed that fibroblast force was the dominant parameter. By contrast, results for $t_{\rho,c}$ and K_t pairings (Fig. 3.7B) suggested that collagen saturation (K_t) had a more pronounced effect coupled to $t_{\rho,c}$ at lower K_t values. For example, when $K_t = 0.1$, cavity contraction values ranged between 25% and 30% for $t_{\rho,c} \in [1 \cdot t_\rho, 2.5 \cdot t_\rho]$. A broader cavity contraction range was observed for $K_t = 0.5$, with values varying from 50% to 37.5% across $t_{\rho,c} \in [1 \cdot t_\rho, 2.5 \cdot t_\rho]$.

The rate of plastic deformation (τ_{λ^p}) was inversely related to cavity contraction. In other words, lower values of τ_{λ^p} supported larger cavity contraction. The contour plot showing τ_{λ^p} and t_ρ pairings (Fig. 3.7C) revealed that cavity contraction was less sensitive to τ_{λ^p} for lower t_ρ values. However, as t_ρ increased, the rate of plastic deformation became more influential on contraction outcomes. For the τ_{λ^p} versus $t_{\rho,c}$ contour (Fig. 3.7D), it was found that myofibroblast force was tightly coupled to the rate of plastic deformation, with cavity contraction becoming more severe for lower τ_{λ^p} and larger $t_{\rho,c}$ values. Interestingly, the greatest cavity contraction (between 20% to 25%) occurred when both τ_{λ^p} and $t_{\rho,c}$ had larger values.

3.3.5 Effect of cavity-to-breast volume percentage (CBVP)

Since the mechanobiological model was informed based on human BCS cavity contraction data, it can be applied to predict how patient-to-patient variability in breast and tumor characteristics affect healing and cosmetic outcomes. For example, the effect of CBVP was evaluated to identify trends in spatiotemporal cavity contraction and breast deformation. This model application involved adding CBVP as an input variable to the established mechanobiological GP. Similar to the initial GP model calibration, LHS sampling of the parameters Θ_m and CBVP was performed. Following GP model re-calibration, 2,500 GP predictive contraction curves were then used to evaluate the 4-week post-surgical cavity contraction and breast deformation for CBVP values between 0.43% and 8.7% (Fig. 3.8A).

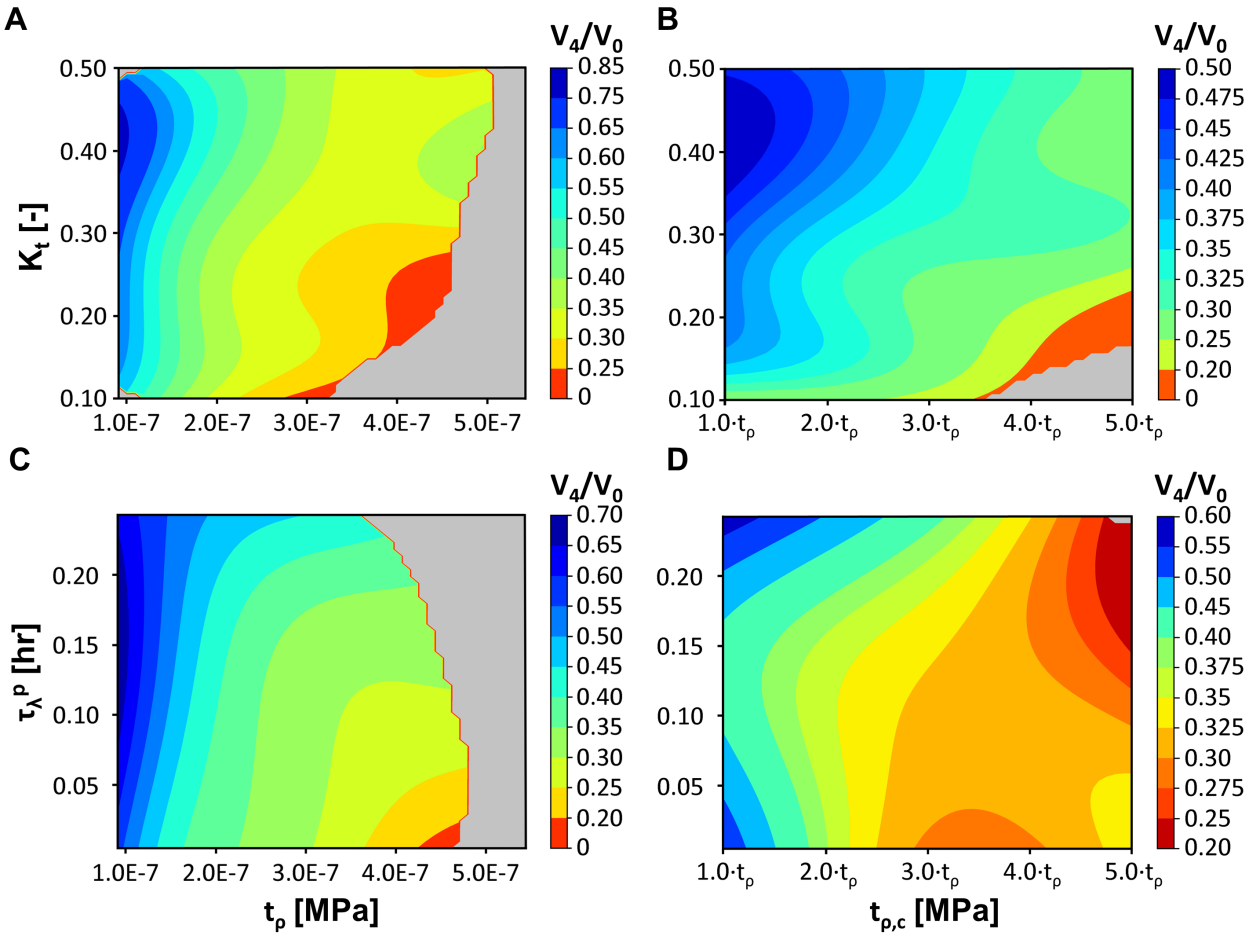

Figure 3.7. Plots showing relationships between uninformed parameters t_ρ, $t_{\rho,c}$, K_t, and τ_{λ^p}. Plots were created based on predictive cavity contraction curves generated using the mechanobiological GP by varying two of the four parameters (constants used: $t_\rho = 1.5 \times 10^{-5}$ MPa, $t_{\rho,c} = 2.5 \cdot t_\rho$ MPa, $K_t = 0.3$, and $\tau_{\lambda^p} = 0.1$ hr) and evaluating the change in cavity volume at week 4. Gray regions on the plots represent regions in the parameter space that were not well informed by the mechanobiological GP.

This CBVP range was based on geometric constraints of the assumed breast geometry and captures the wide range of reported breast tumor sizes [76].

Simulation results showed that smaller cavities contract at a faster rate compared to larger cavities, which is consistent with previously reported human wound contraction outcomes [77], [78]. Additionally, larger CBVP values showed a greater reduction in cavity volume (i.e., greater contracture). Finite element simulations were also conducted for spe-

cific CBVP values of i) 8.7%, ii) 4.5%, iii) 1.0% to verify accuracy of GP predictions and visualize breast deformations (Fig. 3.8B). As expected, permanent changes in breast volume and shape increased with cavity size, with similar permanent deformation values within the cavity centers (3.8B). Overall, larger breast surface deformation occurred with increasing CBVP. For instance, for a relatively small CBVP of 1.0%, there was no visible breast surface deformation 4 weeks post-surgery (3.8B). Increasing the CBVP to 4.5% resulted in moderate surface deformation, which became more severe for CBVP of 8.7% (3.8B). These results are consistent with reported clinical outcomes [15], [79], [80].

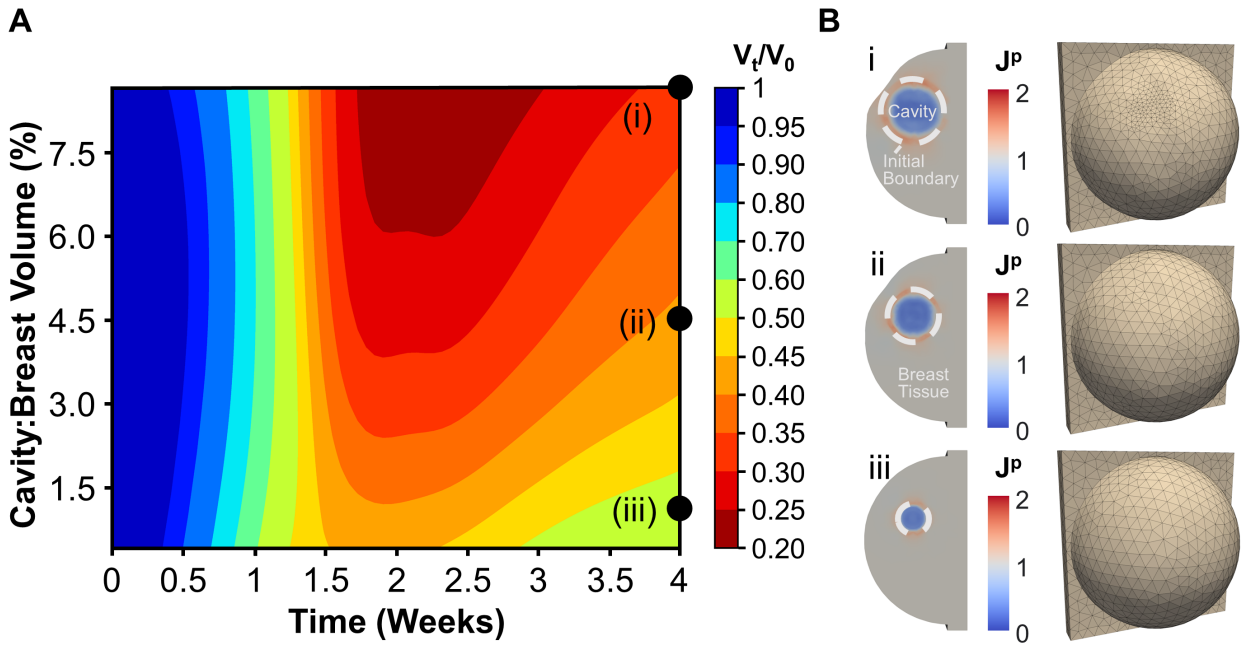

Figure 3.8. Effect of CBVP on cavity contraction and breast surface deformities. (A) Plot was created using optimized mechanobiological parameters while varying CBVP and assessing time-dependent cavity contraction. (B) Breast contour plots displaying permanent tissue deformation and breast surface deformation 4 weeks following lumpectomy for CBVPs of (i) 8.7%, (ii) 4.5%, (iii) and 1.0%.

3.3.6 Effect of Breast Composition

To determine the effect of breast composition on BCS outcomes, the GP surrogate was further informed by running additional simulations including breast composition as an input

variable. Specifically, recall that the material parameters k_0, k_1 were assigned based on the assumption of 70% adipose tissue and 30% fibroglandular tissue [40]. When evaluating the effect of breast composition, k_0, k_1 were modified according to the rule of mixtures by varying the percent of adipose to fibroglandular tissue. Following re-calibration, the GP model was used to predict 4-week post-surgical cavity contraction as a function of breast composition (Fig. 3.9.A). Clinically, breast composition is measured with the BI-RADS ranking system which reports the percentage of breast fibroglandular tissue [41]. As shown in 3.9A, cavities created in low density breasts (i.e., breasts consisting primarily of soft fatty tissue or scattered small regions of fibroglandular tissue) contracted more rapidly and to a greater extent than those in high density breasts (i.e., breasts consisting of heterogeneously or extremely dense fibroglandular tissue). Lower density breasts also gave rise to higher magnitudes of permanent contracture within the cavity, causing the surrounding breast tissue to be drawn in higher tension (Fig. 3.9B). Interestingly, permanent contracture was positively correlated with breast surface deformation, as lower breast densities were more prone to breast asymmetry (Fig. 3.9B). These results are consistent with clinical findings [14], [67], [68], [81].

3.4 Discussion

Understanding the mechanobiology of breast cavity healing after lumpectomy is essential for improved prediction of post-surgical outcomes and individualized treatment planning for breast cancer patients. At present, there is a relatively high incidence of BCS-related breast deformities, with approximately one-third of women developing dents, distortions, and asymmetry between breasts [13]–[16], which negatively impacts survivor self-esteem or quality of life [5]. While the significance of this problem has been recognized by the breast surgical community, there remains a fundamental lack of mechanistic and objective tools that define how various patient-to-patient factors affect post-surgical cavity healing and cosmetic outcomes. In this study, we developed a detailed finite element model of breast cavity healing after BCS that was calibrated using experimental porcine lumpectomy and previously published human clinical data. The computational model incorporated biological,

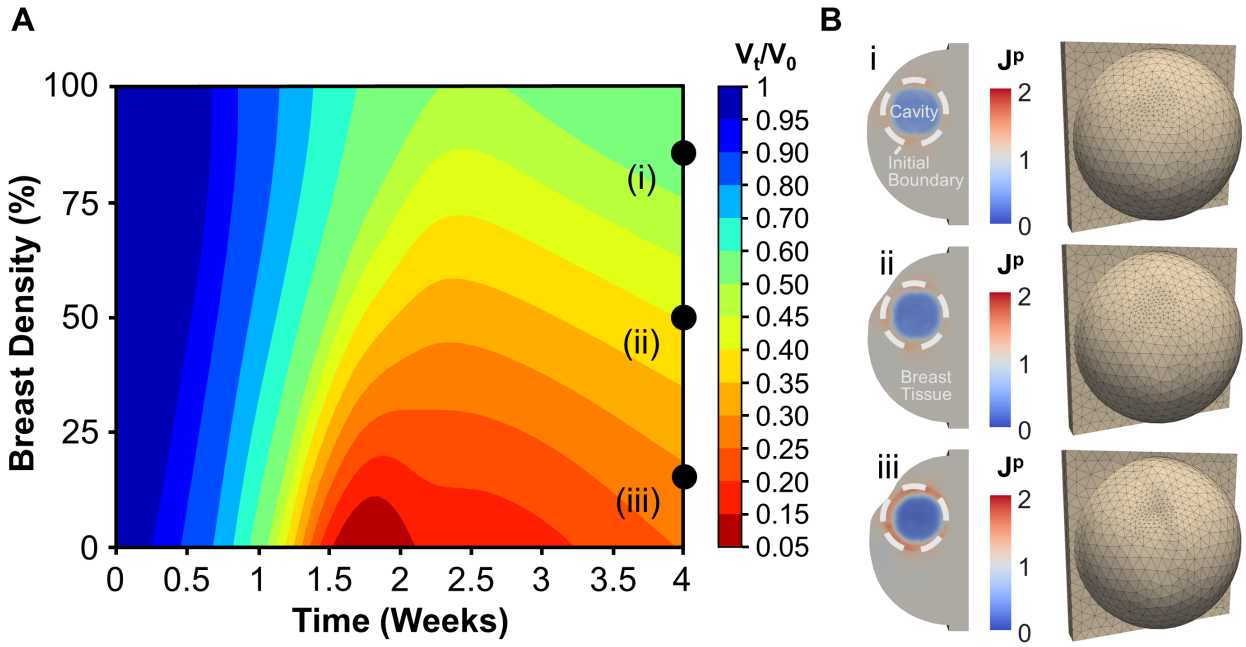

Figure 3.9. Effects of breast density on cavity contraction and breast surface deformities. (A) Plot was created using optimized mechanobiological parameters while varying breast density and assessing time-dependent cavity contraction. (B) Breast contour plots displaying permanent tissue deformation and breast surface deformation four weeks post-surgery for breast densities of (i) 85%, (ii) 50%, and (iii) 15%.

microstructural, and mechanical variables that describe fundamental breast healing processes and relationships. The finite element model was designed to define how the coupling of mechanobiological cues and patient-specific breast characteristics (geometry, consistency, and biomechanics) contributes to temporal changes in cavity contraction and associated breast volume and surface deformations. Therefore, this model has the potential to help both surgeons and patients anticipate BCS healing and cosmetic outcomes.

Computational and mathematical descriptions of wound healing processes and outcomes have been a focus area of investigation for over three decades, with the majority of models describing cutaneous (skin) repair [70], [82]. The first wound healing model, proposed by Sherratt and Murray (1990) [83], did not consider mechanobiology or tissue mechanics when describing re-epithelialization of skin. For this early model, activation and proliferation of

epithelial cells was assumed to occur along a 1D wound in response to chemical cues. Such models have been refined over time to include more complex cellular and chemical reaction-transport phenomena associated with inflammation and angiogenesis [52], [56]. Increasing attention has also been given to fibroblast and myofibroblast activity and their impact on collagen deposition and remodeling [84], [85]. Coupling to nonlinear tissue mechanics has been explored extensively by our group and others in recent years [29]–[31], [52], [54]–[56], [86]. Specifically, our published models have leveraged prior modeling efforts and focused on adding detailed descriptions of local mechanobiological couplings between (myo)fibroblast activity and collagen remodeling to explain the observed macroscale changes in tissue mechanics and elastoplastic deformation. Our extensive work on the calibration of the 3D dermal model based on data from rat excisional wounds showed the model's ability to predict a large set of experimental observations including treatment with collagen scaffolds, providing confidence in the fundamental relationships encoded in the model [31].

Here, we describe a finite element model of breast cavity healing following BCS that builds upon our previously published computational mechanobiological models of cutaneous wound healing [29]–[31]. At present, there are few models describing the healing of deep wounds, such as those associated with BCS, with the majority being adapted from early skin wound models. For example, with the goal of predicting wound healing following lumpectomy, Garbey and co-workers developed a 2D cellular automata model linked to a PDE describing cytokine signaling within skin wounds [26], [86]. Likewise, Vavourakis et al. adapted a finite element model of inflammation and angiogenesis initially introduced by Sherratt and Murray, coupling it with a finite element model of soft tissue biomechanics [28], [87]. In the present study, we modified our 3D dermal wound model [31] to include more realistic fibroblast migration, with dependence on both cytokine concentration and collagen density. We also implemented a generalized breast geometry that was based on human clinical data and adjusted tissue mechanical properties based on the literature. Biochemical and mechanobiological model parameters that were not well defined in the literature were tuned and optimized, allowing the computational model to be fit to experimental porcine lumpectomy data describing time-dependent changes in fibroblast migration and collagen deposition and human clinical data depicting the volumetric breast cavity changes that occur after BCS.

The calibrated model was designed to provide a new and useful tool for supporting future hypothesis generation, surgical visualization, and surgical decision-making. More specifically, we applied the model to define how patient-to-patient variability in breast and tumor characteristics affected breast contracture and breast surface deformation. When evaluating CBVP, model simulations predicted that larger cavities, specifically located within the outer quadrant of the breast, would contract more slowly but to a greater extent than smaller cavities. Additionally, as CBVP increased from 1.0% (13.24 cm^3 volume; 2.94 cm diameter) to 8.7% (115.5 cm^3; 6.04 cm diameter), resultant tissue permanent deformation profiles contributed to more severe breast distortions. These model predictions aligned well with previously published clinical perspectives that state that tumor size, breast tissue volume excised, and EBVP are major determinants of BCS cosmetic outcomes. Maximum tumor diameters between 2 cm and 4 cm are commonly used as selection criteria for BCS [80], [88]. Moreover, EBVP is highly correlated with breast cosmesis assessment scores and patient satisfaction following BCS. Specifically, more than 80% of women were very satisfied with breast aesthetic outcomes when their EBVP was less than 10% [15], [79], [80]. By contrast, EBVP greater than 20% led to high levels of patient dissatisfaction [15], [79], [80]. Tumor location is an important determinant of cosmetic outcomes and patient satisfaction following BCS, with proposed recommendations for maximum EVBP including the following: 18-19% for the upper-outer quadrant, 14-15% for the lower-outer quadrant, 8-9% for the upper-inner quadrant, and 9-10% for the lower-inner quadrant [24]. Such findings have led to proposed surgical decision-making algorithms, where breast volume, clinical tumor size, and tumor location serve as major determinants when choosing between breast surgical procedures to achieve satisfactory breast cosmesis and quality of life [13], [24]. While these algorithms are currently being evaluated in randomized controlled trials in patients who are candidates for both BCS and mastectomy, they fail to incorporate other important patient-specific factors, for example coupling to breast consistency.

Model simulations were also used to determine how breast tissue density affected breast tissue contracture and breast shape following BCS. Human breasts, as well as other mammalian mammary glands, are composed of a heterogeneous mixture of fibroglandular and adipose tissue, which contributes to differences in consistency and biomechanical properties.

Reported Young's modulus ranges for human breasts vary from 0.7 to 66 kPa, depending on breast composition (e.g., percentage of fibroglandular to adipose tissue) [33], [73]. Model simulations evaluated breast densities representing 15% (E_{BT} = 14.5 kPa), 50% (E_{BT} = 25 kPa), and 85% (E_{BT} = 35.5 kPa), spanning the range of soft breast consisting primarily of fatty tissue to firm (stiff) breast consisting primarily of fibroglandular tissue. Our simulations predicted that cavities within low density, fatty breasts exhibit larger contracture compared to high-density, firm breasts. As a result, breast surface deformities were larger and more pronounced as breast density decreased. These results are in agreement with human clinical findings, as many studies have correlated through patient surveys and clinical analysis that patients with low breast density have higher chances of poor cosmetic results and low patient satisfaction after BCS [14], [67], [68], [81].

Mechanobiological parameters influencing cell contractility and plastic deformation were also proven to greatly impact cavity contracture and cosmetic outcomes. Through the sensitivity analysis shown in Figure 3.7, we were able to learn more about plausible parameter ranges and gain insight into complex parameter relationships. The parameters that were deemed to be the most sensitive to the mechanobiological response and contracture were t_ρ and $t_{\rho,c}$. Therefore, it is important to ensure model accuracy regarding these two parameters. Both t_ρ and $t_{\rho,c}$ were optimized based on clinical data evaluating time-dependent cavity volume changes. Compared to dermal wound healing models that considered fibroblast traction based on experimental evidence, our model's optimized value for t_ρ was on the lower end of the established range [30], [31], [52], [55], [56], [85], [86]. Relative to the contractility of fibroblasts, the optimized $t_{\rho,c}$ value for our model was also well within the broad range of values in other wound healing models [30], [31], [52], [55], [56], [85], [86]. To potentially reduce model uncertainty, future experimental studies could be conducted to measure and validate the contractile force of fibroblasts and myofibroblasts post-lumpectomy.

The present study was made possible by leveraging machine learning techniques to replace the high-fidelity computational model with inexpensive but accurate surrogates. In particular, GP surrogates were used to predict cell density, collagen density, and cavity contraction over time as a function of model parameters [89]–[91]. While a single simulation with the fully coupled model takes on the order of 20-72 hours to run (depending on model pa-

rameters), the GP evaluation can be performed in milliseconds. Therefore, this 10^7 speed-up was crucial to perform the parameter optimization and sensitivity analysis. Although many machine learning techniques exist, the GP was applied due to its Bayesian construction which allows the estimation of both the desired quantity of interest and expected epistemic uncertainty (i.e., it provides an estimate of the confidence for a given prediction) [51]. This differentiates GP approaches from other popular tools such as artificial neural networks [51]. The prediction of the variance by the GP guided the selection of parameter combinations for which to evaluate the finite element model, akin to other active learning strategies using GPs [92].

The study is not without limitations. For the computational model, we implemented a generic human breast geometry that was informed through several clinical studies. Further, the model was calibrated by tuning mechanobiological parameters to fit clinical data of time-dependent cavity volume changes reported as an average of 34 patients. Future model iterations will incorporate more patient-specific data, which includes application of patient-specific breast geometries, tumor or cavity shapes and locations, and heterogeneous breast tissue compositions. Individual healing outcomes can then be compared to model predictions to further validate the model. Figure 3.10 shows an example of how the generalized human breast geometry can nonetheless be used to forecast possible poor cosmetic outcomes that patients may experience. The model also fails to incorporate other factors that can affect breast healing. For example, radiation therapy, which is commonly applied to patient breasts shortly after BCS, is not accounted for in the model. This is an area we hope to capture in future work. Addition of radiation therapy to the computational model would require changes cell death, inflammation, collagen deposition, and (myo)fibroblast contraction, ultimately leading to changes in mechanical properties and breast deformation. Although the mechanobiological model is able to accurately predict healing outcomes, the complexity of the model can be further expanded to include additional specific cellular players and processes such as neovascularization, various types of immune cells (e.g., macrophages or neutrophils), and edema related osmotic pressure and poroelastic response. Future model applications also include the design of therapeutic approaches (e.g., regenerative breast tis-

sue fillers), enabling the promise of in silico trials for BCS before animals or human subjects are involved.

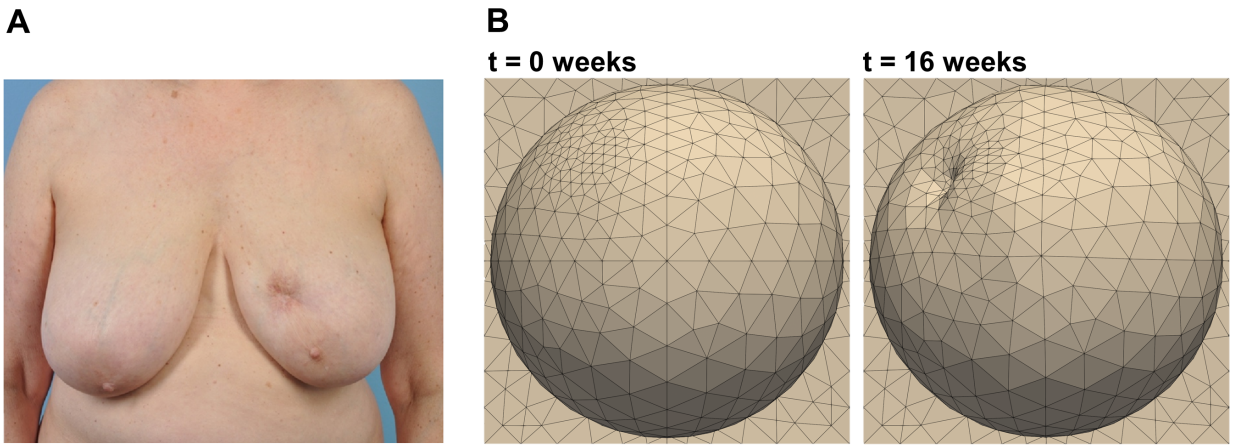

Figure 3.10. Comparison in the cosmetic outcomes after BCS between (A) a patient 5 years removed from BCS and (B) the generalized human breast geometry simulated 16 weeks post-surgery. (A) is reprised from Adamson et al. (2020) [93].

3.5 Conclusions

The presented computational model proved to effectively simulate the breast healing response following BCS, including fibroblast infiltration, collagen remodeling, and breast permanent deformation. Preclinical porcine data and human clinical data were used to inform time-dependent trends for fibroblast density, collagen density, and cavity volume change. The model was fit to this data by optimizing model parameters enabled by GP regression. Although previous models of wound healing after BCS have been developed, we advanced these efforts by implementing a detailed mechanobiological model coupled with the nonlinear mechanics of breast tissue, including large plastic deformation and collagen remodeling. Therefore, our model is uniquely suited for the prediction of scar tissue formation and breast deformation after BCS, which allowed us to gain insight into how key parameters and patient-to-patient variability with respect to breast and tumor characteristics factor into the post-surgical cosmetic outcome. With this work presenting the foundation of the computational model, future efforts can be shifted to focus on patient-specific cases, addition

of radiation therapy effects, and the design of therapeutic approaches (e.g., regenerative breast fillers).

3.6 Appendix: Supplementary Material

The finite element model is available in the following repository: https://github.com/zharbin/CBM_2023_BCS.

Table 3.3. Parameters for the biochemical model. Parameters listed as estimated were selected in this work or modified from our previous wound healing models [30], [31].

Parameter	Description	Value	Reference
D_c $[mm^2/hr]$	Cytokine Diffusion Coefficient	0.01208	[54]–[56]
$d_{\rho,c}$ $[mm^2/hr]$	Cytokine-Increased Fibroblast Diffusivity	6.12×10^{-3}	Estimated
$d_{\rho,0}$ $[mm^2/hr]$	Baseline Fibroblast Diffusivity	6.12×10^{-5}	[85]
p_ρ $[1/hr]$	Fibroblast Proliferation	9×10^{-4}	Estimated
$K_{\rho,c}$ [-]	Proliferation Saturation due to Cytokine	1×10^{-5}	[30]
$p_{\rho,e}$ $[1/hr]$	Mechanoregulation of Fibroblast Proliferation	$p_\rho/2$	[31]
$K_{\rho,\rho}$ [-]	Fibroblast Division Saturation	$550, 512.6$	[52]
d_ρ $[1/hr]$	Fibroblast Death Rate	$p_\rho(1 - \rho_{phys}/K_{\rho\rho})$	[52]
$p_{c,\rho}$ $[1/hr]$	Fibroblast Secretion of Cytokine	1.635×10^{-18}	[30]
$p_{c,e}$ $[1/hr]$	Mechanoregulation of Cytokine	5.45×10^{-18}	[30]
$K_{c,c}$ $[mol/mm^3]$	Cytokine Saturation	1	[30]
d_c $[1/hr]$	Cytokine Death Rate	0.005	Estimated
ρ_0 $[cells/mm^3]$	Nominal Fibroblast Density	55051	Estimated
c_0 $[g/mm^3]$	Initial Cytokine Concentration Inside Cavity	1×10^{-4}	[30]

Table 3.4. Parameters for the fully coupled mechanobiological model. Parameters listed as estimated were selected in this work or modified from our previous wound healing model [30], [31].

Parameter	Description	Value	Reference
k_0 $[MPa]$	Linear Stiffness	6.375×10^{-3}	Estimated
k_1 $[MPa]$	Compressibility	0.317	Estimated
k_f $[MPa]$	Fiber Stiffness	0.015	[59]
k_2 [-]	Nonlinear Stiffening	0.048	[59]
γ_e [-]	Shape of Mechanosensing Curve	5	[30]
ϑ_e [-]	Midpoint of Mechanosensing Curve	2	[30], [60]
$K_{t,c}$ $[-]$	Traction Saturation due to Cytokine	1×10^{-5}	[30]
$K_{\phi,c}$ $[-]$	Collagen Production Saturation due to Cytokine	1×10^{-4}	[30]
p_{ϕ_e} $[1/hr]$	Collagen Production Activated by Stretch	p_ϕ	[30]
$K_{\phi,\rho}$ $[-]$	Collagen Production Saturation due to Collagen Fraction	$(\rho_0 * p_\phi)/d_\phi - 1$	[30]
d_ϕ $[1/hr]$	Collagen Degradation	9.7×10^{-4}	[61]
$d_{\phi,c}$ $[1/hr]$	Collagen Degradation Activated by Cytokine	8.81×10^{-5}	[61]
τ_ω $[hr]$	Time Constant for Reorientation	$10/(K_{\phi,\rho} + 1)$	[30]
τ_κ $[hr]$	Time Constant for Dispersion	$1/(K_{\phi,\rho} + 1)$	[30]
γ_κ [-]	Shape of Dispersion Rate Curve	2	[30]

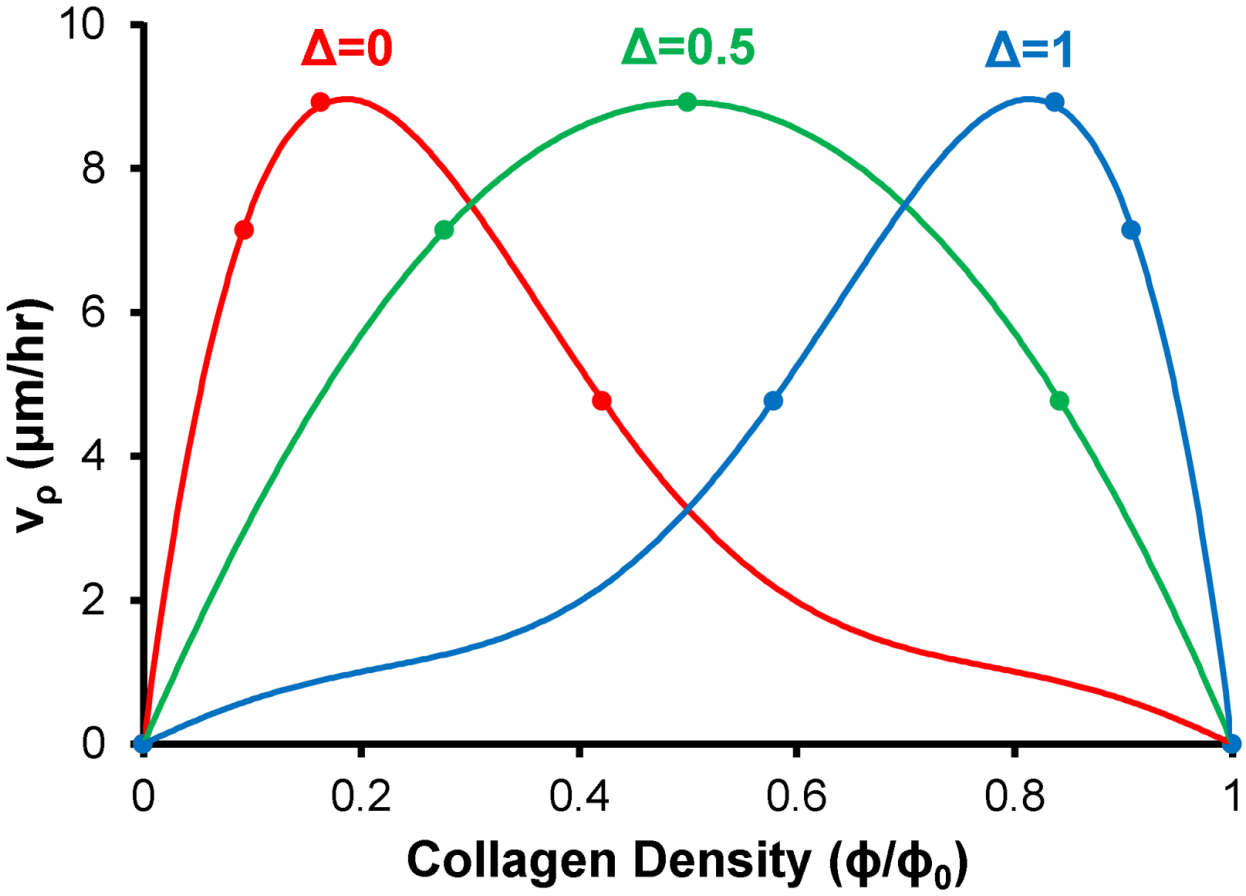

Figure 3.11. Fibroblast speed with respect to collagen density ($v_\rho(\phi)$) and its dependency on Δ. Example $v_\rho(\phi)$ curves are shown with Δ= 0 (red), 0.5 (green), 1 (blue). The function $v_\rho(\phi)$ was initially informed through [12], [72] through 5 data points displayed on the line $\Delta = 0$ while assuming $v_\rho(\phi) = 0$ for ϕ= 0 and 1. Due to the limited data and uncertainty, parameter Δ was created to shift the 5 data points and skew the interpolated function. Δ was further investigated in the biochemical GP, where it was determined that the optimum value was $\Delta = 0$.

Histological Image Analysis Methodology

Quantifying Fibroblast Density

1. Count Red Blood Cells (RBC)
    (a) Adjust Color Balance ([Minimum, Maximum])
        i. Red: [0,0]
        ii. Green: [0,100]
        iii. Blue: [0,0]
    (b) Convert Image Type From RGB Color to 32-bit
    (c) Apply Threshold ([0,$\sim$ 220])
    (d) Apply Watershed Segmentation
    (e) Analyze Particles for RBC Count
        i. Cell Size ([Minimum, Maximum]): [4,∞]
2. Count All Cells
    (a) Adjust Color Balance ([Minimum, Maximum])
        i. Red: [70,220]
        ii. Green: [0,0]
        iii. Blue: [0,0]
    (b) Convert Image Type From RGB Color to 32-bit
    (c) Apply Threshold ([0,$\sim$ 245])
    (d) Apply Watershed Segmentation
    (e) Analyze Particles for All Cell Count
        i. Under "Set Measurements" Select Original Slide Under "Redirect to:"
        ii. Cell Size ([Minimum, Maximum]): [4,∞]
    (f) Evaluate Modal Gray Value ($\leq\sim$125) to Isolate and Count Immune Cells
3. Fibroblast Count = All Cell Count - RBC Count - Immune Cell Count

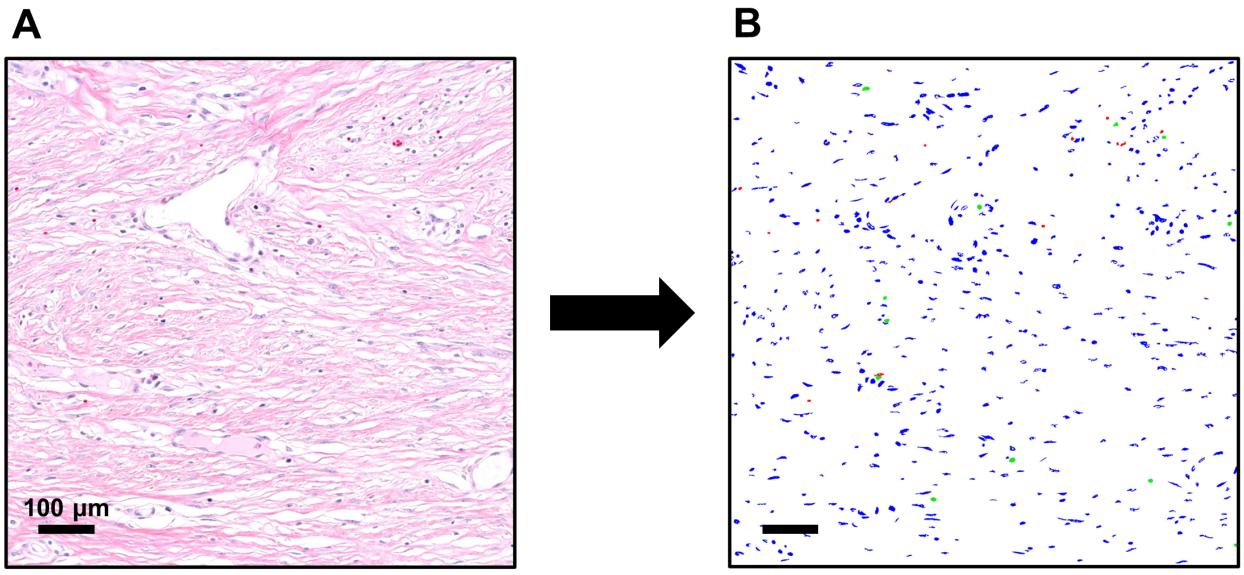

Figure 3.12. Result of post-processing individual regions (500 x 500 μm^2) obtained from porcine lumpectomy histology slides. (A) Regions were captured through Aperio ImageScope sampling across the entire cavity domain. Pictured is an example region from a histology slide 16 weeks post-surgery. (B) Using the procedures described above, regions were processed in ImageJ to quantify the number of fibroblasts (blue), red blood cells (red), and immune cells (green).

Calculating Collagen Density

1. In the 500 x 500 μm^2 histology region, select a small rectangular area ($\sim$100 μm^2) that contains no cells.

2. Measure for average pixel intensity in the small rectangular area. Note: Pixel intensity varies between 0 (black) and 255 (white).

3. Repeat steps 1 and 2 for a 500 x 500 μm^2 histology region that contains healthy breast connective tissue.

4. Calculate the estimated collagen density through the following equation:

$$(\phi/\phi_0)_{est.} = \frac{I_{scar}-255}{0.3*(I_{connective}-255)}$$

   where I_{scar} is the intensity of the scar tissue at the analyzed week and $I_{connective}$ is the intensity of the connective tissue.

4. CONCLUSION

4.1 Summary

Breast cancer impacts millions of women across the world. The current standard of care for breast cancer, breast-conserving surgery, preserves healthy breast tissue by only removing the cancerous tumor surrounded by a small negative margin. This creates a breast cavity that undergoes the wound healing process, leading to scar formation and the contraction of the cavity. As a result, BCS patients often experience post-surgical breast deformities, such as breast asymmetry or the shaping of a divot/dent, which can negatively affect the patient's quality of life. However, due to the complexity of the wound healing process and patient-to-patient variability, it can be difficult for surgeons to preoperatively predict negative healing outcomes. As a solution, our goal was to develop an informed, predictive computational mechanobiology model that simulates breast healing following BCS. The work in this thesis bridges the gap between computational modeling and clinical evidence to help better inform surgeons and patients of oncologic, healing, and cosmetic outcomes post-lumpectomy.

The computational mechanobiological model was initially designed to explore 3D cutaneous wound healing but was adapted and modified for this work to be breast-specific. This was done through an extensive literature review, as we used clinical data to inform the breast tissue material properties, breast tissue composition, and cavity location. Furthermore, a unique generalized breast geometry was created based on available clinical data that analyzed the contraction of a breast cavity after whole-breast irradiation. Mechanobioloigcal parameters were informed through the Gaussian Process by fitting the model to data evaluating time-dependent cavity volume changes post-irradiation. These results provided definition of key model parameters and relationships, allowing for proper calibration of breast cavity contraction.

Next, we evaluated histological cross-sections from an experimental porcine lumpectomy study to find time-dependent changes in fibroblast and collagen density. This information was used for further model calibration by optimizing biochemical parameters to fit experimental fibroblast and collagen data through the GP. Mechanobiological parameters were then informed through a similar process as before, but with the use of human clinical post-

surgical cavity contraction data beginning directly after surgery. With the optimized model, we were able to give insight into how model parameters and patient-to-patient variability regarding breast and tumor characteristics contribute to the post-surgical cosmetic outcome.

Overall, the validity of the model with respect to preclinical and clinical data allowed for accurate finite element simulations evaluating the breast healing response following BCS, including fibroblast infiltration, collagen remodeling, and breast permanent deformation. The mechanistic nature of the model and its fit to porcine and human data are encouraging for future work and applications.

4.2 Future Work

4.2.1 Patient-Specific Applications

For the presented computational model, we implemented a generic human breast geometry that was based on averages from specific clinical studies. Through this, we were able to run finite element simulations using the geometry to fit the study's reported time-dependent cavity volume changes, which allowed for the tuning of mechanobiological parameters. For future iterations of the model, we wish to use more patient-specific data, which includes applying a patient-specific breast geometry, individual tumor/cavity shape and location, and heterogeneous breast tissue composition. This would allow for further model validation by comparing patient-specific healing and cosmetic outcomes to the model predictions.

4.2.2 Whole-Breast Irradiation

In future work, we also plan to investigate outside factors that can possibly affect the wound healing process. Specifically, we will look to integrate whole-breast irradiation, which is commonly undergone by patients shortly after BCS, into the model. Irradiation treatment can greatly impact the normal process of wound healing, causing additional cell death, a decrease in collagen deposition, and stimulating cytokine secretion. Furthermore, it can also cause dramatic changes in the extracellular matrix, thus causing changes in breast tissue material properties. On top of the contraction due to the normal healing process, whole-

breast irradiation causes further contraction of the cavity. This topic was explored in-depth in Chapter 2 through a comprehensive literature review.

4.2.3 Preclinical and Clinical Model Validation

We also aim to continue to use preclincial and clinical data to continue to validate and inform the computational model. For example, two mechanobiological parameters that were found to be sensitive to the mechanobiological response and cavity contracture were the contractile force of fibroblasts and myofibroblasts. Therefore, it is important to ensure model accuracy regarding these two parameters. In the current iteration of the model, both parameters were optimized based on clinical data evaluating time-dependent cavity volume changes. To potentially reduce model uncertainty, future experimental studies could be conducted to measure and validate the contractile force of fibroblasts and myofibroblasts post-lumpectomy. We also wish to use the computational model to explore the design of therapeutic approaches (e.g., regenerative breast fillers), enabling the promise of *in silico* trials for BCS before animal or human subjects are involved. By using data obtained from the porcine lumpectomy study performed by our group, the model could be calibrated to replicate wound healing results using a collagen filler compared to the standard untreated defects.

4.3 Conclusion

The work in this thesis presented the framework for a computational mechanobiological model aimed to simulate breast healing following BCS. In using preclinical porcine data and human clinical data, model parameters and geometry characteristics were informed, which allowed for the calibration of the model. The computational model coupled with nonlinear mechanics of breast tissue, such as plastic deformation and collagen remodeling, made it uniquely suited for the prediction of oncologic, healing, and cosmetic outcomes after BCS. This allowed for the evaluation of model parameters and patient-specific breast and tumor characteristics and their impact on the post-surgical cosmetic outcome. Future modeling efforts look to build upon the presented work by continuing to increase the model complexity

in hopes of capturing an accurate representation of patient-specific cavity healing. In the future, the computational model has the potential to become a tool to inform both surgeons and patients through the creation of individualized patient treatment plans that lead to decreased post-surgical complications and improved patient quality of life.

REFERENCES

[1] A. N. Giaquinto, H. Sung, K. D. Miller, *et al.*, "Breast cancer statistics, 2022," *CA: A Cancer Journal for Clinicians*, vol. 72, no. 6, pp. 524–541, 2022.

[2] *Cancer of the breast (female) - cancer stat facts*. [Online]. Available: https://seer.cancer.gov/statfacts/html/breast.html.

[3] M. S. Moran, S. J. Schnitt, A. E. Giuliano, *et al.*, "Society of surgical oncology–american society for radiation oncology consensus guideline on margins for breast-conserving surgery with whole-breast irradiation in stages i and ii invasive breast cancer," *International Journal of Radiation Oncology* Biology* Physics*, vol. 88, no. 3, pp. 553–564, 2014.

[4] R. Chow, N. Pulenzas, L. Zhang, *et al.*, "Quality of life and symptom burden in patients with breast cancer treated with mastectomy and lumpectomy," *Supportive Care in Cancer*, vol. 24, pp. 2191–2199, 2016.

[5] J. de Boniface, R. Szulkin, and A. L. Johansson, "Survival after breast conservation vs mastectomy adjusted for comorbidity and socioeconomic status: A swedish national 6-year follow-up of 48 986 women," *JAMA Surgery*, vol. 156, no. 7, pp. 628–637, 2021.

[6] A. Chatterjee, B. Pyfer, B. Czerniecki, K. Rosenkranz, J. Tchou, and C. Fisher, "Early postoperative outcomes in lumpectomy versus simple mastectomy," *journal of Surgical Research*, vol. 198, no. 1, pp. 143–148, 2015.

[7] S. Litière, G. Werutsky, I. S. Fentiman, *et al.*, "Breast conserving therapy versus mastectomy for stage i–ii breast cancer: 20 year follow-up of the eortc 10801 phase 3 randomised trial," *The Lancet Oncology*, vol. 13, no. 4, pp. 412–419, 2012.

[8] H. D. Mogal, C. Clark, R. Dodson, N. F. Fino, and M. Howard-McNatt, "Outcomes after mastectomy and lumpectomy in elderly patients with early-stage breast cancer," *Annals of Surgical Oncology*, vol. 24, pp. 100–107, 2017.

[9] E. Hau, L. Browne, A. Capp, *et al.*, "The impact of breast cosmetic and functional outcomes on quality of life: Long-term results from the st. george and wollongong randomized breast boost trial," *Breast Cancer Research and Treatment*, vol. 139, pp. 115–123, 2013.

[10] J. F. Waljee, E. S. Hu, P. A. Ubel, D. M. Smith, L. A. Newman, and A. K. Alderman, "Effect of esthetic outcome after breast-conserving surgery on psychosocial functioning and quality of life," *Journal of Clinical Oncology*, vol. 26, no. 20, pp. 3331–3337, 2008.

[11] M. J. Cardoso, H. Oliveira, and J. Cardoso, "Assessing cosmetic results after breast conserving surgery," *Journal of Surgical Oncology*, vol. 110, no. 1, pp. 37–44, 2014.

[12] T. J. Puls, C. S. Fisher, A. Cox, *et al.*, "Regenerative tissue filler for breast conserving surgery and other soft tissue restoration and reconstruction needs," *Scientific Reports*, vol. 11, no. 1, p. 2711, 2021.

[13] E. Vos, L. Koppert, W. van Lankeren, C. Verhoef, B. G. Koerkamp, and M. Hunink, "A preliminary prediction model for potentially guiding patient choices between breast conserving surgery and mastectomy in early breast cancer patients; a dutch experience," *Quality of Life Research*, vol. 27, pp. 545–553, 2018.

[14] A. Gardfjell, C. Dahlbäck, and K. Åhsberg, "Patient satisfaction after unilateral oncoplastic volume displacement surgery for breast cancer, evaluated with the breast-q," *World Journal of Surgical Oncology*, vol. 17, pp. 1–13, 2019.

[15] C. Dahlbäck, J. Manjer, M. Rehn, and A. Ringberg, "Determinants for patient satisfaction regarding aesthetic outcome and skin sensitivity after breast-conserving surgery," *World Journal of Surgical Oncology*, vol. 14, pp. 1–11, 2016.

[16] D. F. Veiga, J. Veiga-Filho, L. M. Ribeiro, *et al.*, "Quality-of-life and self-esteem outcomes after oncoplastic breast-conserving surgery [outcomes article]," *Plastic and Reconstructive Surgery*, vol. 125, no. 3, pp. 811–817, 2010.

[17] I. C. Henderson, *Breast cancer: Fundamentals of evidence-based disease management*. Oxford University Press, 2015.

[18] P. G. Cordeiro, "Breast reconstruction after surgery for breast cancer," *New England Journal of Medicine*, vol. 359, no. 15, pp. 1590–1601, 2008.

[19] J. M. Serletti, J. Fosnot, J. A. Nelson, J. J. Disa, and L. P. Bucky, "Breast reconstruction after breast cancer," *Plastic and Reconstructive Surgery*, vol. 127, no. 6, 124e–135e, 2011.

[20] J.-Y. Chen, Y.-J. Huang, L.-L. Zhang, C.-Q. Yang, and K. Wang, "Comparison of oncoplastic breast-conserving surgery and breast-conserving surgery alone: A meta-analysis," *Journal of Breast Cancer*, vol. 21, no. 3, pp. 321–329, 2018.

[21] P. L. Tenofsky, P. Dowell, T. Topalovski, and S. D. Helmer, "Surgical, oncologic, and cosmetic differences between oncoplastic and nononcoplastic breast conserving surgery in breast cancer patients," *The American Journal of Surgery*, vol. 207, no. 3, pp. 398–402, 2014.

[22] A. Chatterjee, A. C. Offodile II, A. Asban, *et al.*, "A cost-utility analysis comparing oncoplastic breast surgery to standard lumpectomy in large breasted women," *Advances in Breast Cancer Research*, vol. 7, no. 2, pp. 187–200, 2018.

[23] E. L. Vos, A. H. Koning, I.-M. Obdeijn, *et al.*, "Preoperative prediction of cosmetic results in breast conserving surgery," *Journal of Surgical Oncology*, vol. 111, no. 2, pp. 178–184, 2015.

[24] D. Pukancsik, P. Kelemen, M. Újhelyi, *et al.*, "Objective decision making between conventional and oncoplastic breast-conserving surgery or mastectomy: An aesthetic and functional prospective cohort study," *European Journal of Surgical Oncology (EJSO)*, vol. 43, no. 2, pp. 303–310, 2017.

[25] B. L. Bass and M. Garbey, "A road map for computational surgery: Challenges and opportunities," *Journal of Computational Surgery*, vol. 1, no. 1, pp. 1–18, 2014.

[26] M. Garbey, R. Salmon, D. Thanoon, and B. L. Bass, "Multiscale modeling and distributed computing to predict cosmesis outcome after a lumpectomy," *Journal of Computational Physics*, vol. 244, pp. 321–335, 2013.

[27] R. Salmon, M. Garbey, L. W. Moore, and B. L. Bass, "Interrogating a multifactorial model of breast conserving therapy with clinical data," *Plos One*, vol. 10, no. 4, e0125006, 2015.

[28] V. Vavourakis, B. Eiben, J. H. Hipwell, N. R. Williams, M. Keshtgar, and D. J. Hawkes, "Multiscale mechano-biological finite element modelling of oncoplastic breast surgerynumerical study towards surgical planning and cosmetic outcome prediction," *PloS One*, vol. 11, no. 7, e0159766, 2016.

[29] A. Buganza Tepole and E. Kuhl, "Computational modeling of chemo-bio-mechanical coupling: A systems-biology approach toward wound healing," *Computer Methods in Biomechanics and Biomedical Engineering*, vol. 19, no. 1, pp. 13–30, 2016.

[30] A. B. Tepole, "Computational systems mechanobiology of wound healing," *Computer Methods in Applied Mechanics and Engineering*, vol. 314, pp. 46–70, 2017.

[31] D. O. Sohutskay, A. B. Tepole, and S. L. Voytik-Harbin, "Mechanobiological wound model for improved design and evaluation of collagen dermal replacement scaffolds," *Acta Biomaterialia*, vol. 135, pp. 368–382, 2021.

[32] L. Han, J. H. Hipwell, C. Tanner, *et al.*, "Development of patient-specific biomechanical models for predicting large breast deformation," *Physics in Medicine & Biology*, vol. 57, no. 2, p. 455, 2011.

[33] A. Gefen and B. Dilmoney, "Mechanics of the normal woman's breast," *Technology and Health Care*, vol. 15, no. 4, pp. 259–271, 2007.

[34] F. S. Azar, D. N. Metaxas, and M. D. Schnall, "Methods for modeling and predicting mechanical deformations of the breast under external perturbations," *Medical Image Analysis*, vol. 6, no. 1, pp. 1–27, 2002.

[35] P. R. Bakic, *Breast tissue description and modeling in mammography*. Lehigh University, 2001.

[36] A. L. McKnight, J. L. Kugel, P. J. Rossman, A. Manduca, L. C. Hartmann, and R. L. Ehman, "Mr elastography of breast cancer: Preliminary results," *American Journal of Roentgenology*, vol. 178, no. 6, pp. 1411–1417, 2002.

[37] T. A. Krouskop, T. M. Wheeler, F. Kallel, B. S. Garra, and T. Hall, "Elastic moduli of breast and prostate tissues under compression," *Ultrasonic Imaging*, vol. 20, no. 4, pp. 260–274, 1998.

[38] A. Samani and D. Plewes, "A method to measure the hyperelastic parameters of ex vivo breast tissue samples," *Physics in Medicine & Biology*, vol. 49, no. 18, p. 4395, 2004.

[39] P. S. Wellman, *Tactile imaging*. Harvard University, 1999.

[40] T. R. Nelson, L. I. Cerviño, J. M. Boone, and K. K. Lindfors, "Classification of breast computed tomography data," *Medical Physics*, vol. 35, no. 3, pp. 1078–1086, 2008.

[41] A. C. of Radiology, C. J. D'Orsi, E. A. Sickles, E. B. Mendelson, E. A. Morris, *et al.*, *ACR BI-RADS atlas: breast imaging reporting and data system; mammography, ultrasound, magnetic resonance imaging, follow-up and outcome monitoring, data dictionary*. ACR, American College of Radiology, 2013.

[42] K. S. Oh, F.-M. Kong, K. A. Griffith, B. Yanke, and L. J. Pierce, "Planning the breast tumor bed boost: Changes in the excision cavity volume and surgical scar location after breast-conserving surgery and whole-breast irradiation," *International Journal of Radiation Oncology* Biology* Physics*, vol. 66, no. 3, pp. 680–686, 2006.

[43] L. H. Kim, F. Vicini, and D. Yan, "What do recent studies on lumpectomy cavity volume change imply for breast clinical target volumes?" *International Journal of Radiation Oncology, Biology, Physics*, vol. 72, no. 1, pp. 1–3, 2008.

[44] B. Prendergast, D. J. Indelicato, S. R. Grobmyer, *et al.*, "The dynamic tumor bed: Volumetric changes in the lumpectomy cavity during breast-conserving therapy," *International Journal of Radiation Oncology* Biology* Physics*, vol. 74, no. 3, pp. 695–701, 2009.

[45] S. Rummel, M. T. Hueman, N. Costantino, C. D. Shriver, and R. E. Ellsworth, "Tumour location within the breast: Does tumour site have prognostic ability?" *Ecancermedicalscience*, vol. 9, 2015.

[46] P. D. Darbre, "Recorded quadrant incidence of female breast cancer in great britain suggests a disproportionate increase in the upper outer quadrant of the breast," *Anticancer Research*, vol. 25, no. 3C, pp. 2543–2550, 2005.

[47] N. Kroman, J. Wohlfahrt, H. T. Mouridsen, and M. Melbye, "Influence of tumor location on breast cancer prognosis," *International Journal of Cancer*, vol. 105, no. 4, pp. 542–545, 2003.

[48] C. Hurkmans, M. Admiraal, M. van der Sangen, and I. Dijkmans, "Significance of breast boost volume changes during radiotherapy in relation to current clinical interobserver variations," *Radiotherapy and Oncology*, vol. 90, no. 1, pp. 60–65, 2009.

[49] T. W. Flannery, E. M. Nichols, S. B. Cheston, *et al.*, "Repeat computed tomography simulation to assess lumpectomy cavity volume during whole-breast irradiation," *International Journal of Radiation Oncology* Biology* Physics*, vol. 75, no. 3, pp. 751–756, 2009.

[50] R. J. Tersteeg, J. M. Roesink, M. Albregts, C. C. Wárlám-Rodenhuis, and B. van Asselen, "Changes in excision cavity volume: Prediction of the reduction in absolute volume during breast irradiation," *International Journal of Radiation Oncology* Biology* Physics*, vol. 74, no. 4, pp. 1181–1185, 2009.

[51] C. E. Rasmussen and C. K. Williams, "Gaussian processes in machine learning," *Lecture Notes in Computer Science*, vol. 3176, pp. 63–71, 2004.

[52] C. Valero, E. Javierre, J. M. Garca-Aznar, and M. J. Gómez-Benito, "A cell-regulatory mechanism involving feedback between contraction and tissue formation guides wound healing progression," *PloS One*, vol. 9, no. 3, e92774, 2014.

[53] K. Ghosh, Z. Pan, E. Guan, *et al.*, "Cell adaptation to a physiologically relevant ecm mimic with different viscoelastic properties," *Biomaterials*, vol. 28, no. 4, pp. 671–679, 2007.

[54] B. D. Cumming, D. McElwain, and Z. Upton, "A mathematical model of wound healing and subsequent scarring," *Journal of The Royal Society Interface*, vol. 7, no. 42, pp. 19–34, 2010.

[55] D. C. Koppenol, F. J. Vermolen, F. B. Niessen, P. P. van Zuijlen, and K. Vuik, "A mathematical model for the simulation of the formation and the subsequent regression of hypertrophic scar tissue after dermal wounding," *Biomechanics and Modeling in Mechanobiology*, vol. 16, pp. 15–32, 2017.

[56] K. E. Murphy, C. L. Hall, P. K. Maini, S. W. McCue, and D. S. McElwain, "A fibrocontractive mechanochemical model of dermal wound closure incorporating realistic growth factor kinetics," *Bulletin of Mathematical Biology*, vol. 74, pp. 1143–1170, 2012.

[57] C. Miller, G. Godeau, C. Lebreton-DeCoster, *et al.*, "Validation of a morphometric method for evaluating fibroblast numbers in normal and pathologic tissues," *Experimental Dermatology*, vol. 12, no. 4, pp. 403–411, 2003.

[58] E. Rognoni, A. O. Pisco, T. Hiratsuka, *et al.*, "Fibroblast state switching orchestrates dermal maturation and wound healing," *Molecular Systems Biology*, vol. 14, no. 8, e8174, 2018.

[59] A. B. Tepole, H. Kabaria, K.-U. Bletzinger, and E. Kuhl, "Isogeometric kirchhoff–love shell formulations for biological membranes," *Computer Methods in Applied Mechanics and Engineering*, vol. 293, pp. 328–347, 2015.

[60] A. B. Tepole, C. J. Ploch, J. Wong, A. K. Gosain, and E. Kuhl, "Growing skin: A computational model for skin expansion in reconstructive surgery," *Journal of the Mechanics and Physics of Solids*, vol. 59, no. 10, pp. 2177–2190, 2011.

[61] G. Laurent, "Dynamic state of collagen: Pathways of collagen degradation in vivo and their possible role in regulation of collagen mass," *American Journal of Physiology-Cell Physiology*, vol. 252, no. 1, pp. C1–C9, 1987.

[62] A. Fourquet, F. Campana, B. Zafrani, *et al.*, "Prognostic factors of breast recurrence in the conservative management of early breast cancer: A 25-year follow-up," *International Journal of Radiation Oncology* Biology* Physics*, vol. 17, no. 4, pp. 719–725, 1989.

[63] E. B. C. T. C. Group *et al.*, "Effects of radiotherapy and of differences in the extent of surgery for early breast cancer on local recurrence and 15-year survival: An overview of the randomised trials," *The Lancet*, vol. 366, no. 9503, pp. 2087–2106, 2005.

[64] M. Azu, P. Abrahamse, S. J. Katz, R. Jagsi, and M. Morrow, "What is an adequate margin for breast-conserving surgery? surgeon attitudes and correlates," *Annals of Surgical Oncology*, vol. 17, pp. 558–563, 2010.

[65] A. Tremelling, R. L. Aft, A. E. Cyr, *et al.*, "Impact of consensus guidelines for breast-conserving surgery in patients with ductal carcinoma in situ," *Cancer Reports*, vol. 5, no. 5, e1502, 2022.

[66] A. L. Pusic, A. F. Klassen, A. M. Scott, J. A. Klok, P. G. Cordeiro, and S. J. Cano, "Development of a new patient-reported outcome measure for breast surgery: The breast-q," *Plastic and Reconstructive Surgery*, vol. 124, no. 2, pp. 345–353, 2009.

[67] P. C. Rassu, "Observed outcomes on the use of oxidized and regenerated cellulose polymer for breast conserving surgery–a case series," *Annals of Medicine and Surgery*, vol. 5, pp. 57–66, 2016.

[68] R. Mitsueda, A. Gen, Y. Fujiki, *et al.*, "Satisfaction of patients who received breast-conserving surgery using the suture scaffold technique: A single-institution, cross-sectional study," *Annals of Surgical Oncology*, vol. 29, no. 6, pp. 3829–3835, 2022.

[69] A. Brands-Appeldoorn, R. Thomma, L. Janssen, A. Maaskant-Braat, V. Tjan-Heijnen, and R. Roumen, "Factors related to patient-reported cosmetic outcome after breast-conserving therapy for breast cancer," *Breast Cancer Research and Treatment*, vol. 191, no. 3, pp. 545–552, 2022.

[70] C. Valero, E. Javierre, J. Garca-Aznar, A. Menzel, and M. Gomez-Benito, "Challenges in the modeling of wound healing mechanisms in soft biological tissues," *Annals of Biomedical Engineering*, vol. 43, pp. 1654–1665, 2015.

[71] M. Pensalfini and A. B. Tepole, "Mechano-biological and bio-mechanical pathways in cutaneous wound healing," *PLOS Computational Biology*, vol. 19, no. 3, e1010902, 2023.

[72] D. O. Sohutskay, T. J. Puls, and S. L. Voytik-Harbin, "Collagen self-assembly: Biophysics and biosignaling for advanced tissue generation," *Multi-scale Extracellular Matrix Mechanics and Mechanobiology*, pp. 203–245, 2020.

[73] N. G. Ramiao, P. S. Martins, R. Rynkevic, A. A. Fernandes, M. Barroso, and D. C. Santos, "Biomechanical properties of breast tissue, a state-of-the-art review," *Biomechanics and Modeling in Mechanobiology*, vol. 15, pp. 1307–1323, 2016.

[74] S. S. Jeffrey, W. H. Goodson, D. M. Ikeda, R. L. Birdwell, and M. S. Bogetz, "Axillary lymphadenectomy for breast cancer without axillary drainage," *Archives of Surgery*, vol. 130, no. 8, pp. 909–913, 1995.

[75] A. Valeta-Magara, R. Hatami, D. Axelrod, *et al.*, "Pro-oncogenic cytokines and growth factors are differentially expressed in the post-surgical wound fluid from malignant compared to benign breast lesions," *SpringerPlus*, vol. 4, no. 1, pp. 1–11, 2015.

[76] H. G. Welch, P. C. Prorok, A. J. OMalley, and B. S. Kramer, "Breast-cancer tumor size, overdiagnosis, and mammography screening effectiveness," *New England Journal of Medicine*, vol. 375, no. 15, pp. 1438–1447, 2016.

[77] C. E. Ananian, R. D. Davis, E. L. Johnson, *et al.*, "Wound closure outcomes suggest clinical equivalency between lyopreserved and cryopreserved placental membranes containing viable cells," *Advances in Wound Care*, vol. 8, no. 11, pp. 546–554, 2019.

[78] C. E. Fife, S. D. Horn, R. J. Smout, R. S. Barrett, and B. Thomson, "A predictive model for diabetic foot ulcer outcome: The wound healing index," *Advances in Wound Care*, vol. 5, no. 7, pp. 279–287, 2016.

[79] J. Stevenson, R. Macmillan, S. Downey, L. Renshaw, and J. Dixon, "Factors affecting cosmetic outcome after breast conserving surgery," *European Journal of Cancer*, no. 37, p. 31, 2001.

[80] R. Cochrane, P. Valasiadou, A. Wilson, S. Al-Ghazal, and R. Macmillan, "Cosmesis and satisfaction after breast-conserving surgery correlates with the percentage of breast volume excised," *Journal of British Surgery*, vol. 90, no. 12, pp. 1505–1509, 2003.

[81] N. Shiina, M. Sakakibara, K. Fujisaki, *et al.*, "Volumetric breast density is essential for predicting cosmetic outcome at the late stage after breast-conserving surgery," *European Journal of Surgical Oncology (EJSO)*, vol. 42, no. 4, pp. 481–488, 2016.

[82] J. A. Flegg, S. N. Menon, P. K. Maini, and D. S. McElwain, "On the mathematical modeling of wound healing angiogenesis in skin as a reaction-transport process," *Frontiers in Physiology*, vol. 6, p. 262, 2015.

[83] J. A. Sherratt and J. D. Murray, "Models of epidermal wound healing," *Proceedings of the Royal Society of London. Series B: Biological Sciences*, vol. 241, no. 1300, pp. 29–36, 1990.

[84] R. T. Tranquillo and J. Murray, "Continuum model of fibroblast-driven wound contraction: Inflammation-mediation," *Journal of Theoretical Biology*, vol. 158, no. 2, pp. 135–172, 1992.

[85] L. Olsen, J. A. Sherratt, and P. K. Maini, "A mechanochemical model for adult dermal wound contraction and the permanence of the contracted tissue displacement profile," *Journal of Theoretical Biology*, vol. 177, no. 2, pp. 113–128, 1995.

[86] E. Javierre, P. Moreo, M. Doblaré, and J. Garca-Aznar, "Numerical modeling of a mechano-chemical theory for wound contraction analysis," *International Journal of Solids and Structures*, vol. 46, no. 20, pp. 3597–3606, 2009.

[87] J. A. Sherratt and J. Murray, "Mathematical analysis of a basic model for epidermal wound healing," *Journal of Mathematical Biology*, vol. 29, pp. 389–404, 1991.

[88] J. Gu, G. Groot, C. Boden, A. Busch, L. Holtslander, and H. Lim, "Review of factors influencing women's choice of mastectomy versus breast conserving therapy in early stage breast cancer: A systematic review," *Clinical Breast Cancer*, vol. 18, no. 4, e539–e554, 2018.

[89] I. Bilionis, N. Zabaras, B. A. Konomi, and G. Lin, "Multi-output separable gaussian process: Towards an efficient, fully bayesian paradigm for uncertainty quantification," *Journal of Computational Physics*, vol. 241, pp. 212–239, 2013.

[90] R. Tripathy, I. Bilionis, and M. Gonzalez, "Gaussian processes with built-in dimensionality reduction: Applications to high-dimensional uncertainty propagation," *Journal of Computational Physics*, vol. 321, pp. 191–223, 2016.

[91] M. Raissi, P. Perdikaris, and G. E. Karniadakis, "Machine learning of linear differential equations using gaussian processes," *Journal of Computational Physics*, vol. 348, pp. 683–693, 2017.

[92] F. Sahli Costabal, Y. Yang, P. Perdikaris, D. E. Hurtado, and E. Kuhl, "Physics-informed neural networks for cardiac activation mapping," *Frontiers in Physics*, vol. 8, p. 42, 2020.

[93] K. Adamson, D. D. Rivedal, and E. L. Doren, "Breast reconstruction following breast conserving surgery: A review," *Current Surgery Reports*, vol. 8, pp. 1–10, 2020.